AN EMPIRICAL MODEL OF PIEZOELECTRIC STICK-SLIP ACTUATION OF THE KLEINDIEK MM3A MICROMANIPULATOR

by

Aayush Damani

A thesis submitted to the faculty of
The University of Utah
in partial fulfillment of the requirements for the degree of

Master of Science

Department of Mechanical Engineering

The University of Utah

May 2013

ABSTRACT

The need for precise micro/nano-positioning has arisen in many fields of research and technology. Piezoelectric stick-slip actuators are widely used where precise positioning over a wide range of motion is required. Controlling manipulators that utilize piezoelectric stick-slip actuators is not a trivial task, as these actuators have a discrete stepping nature, with a step size that is influenced by a variety of factors such as actuator loading, temperature, and humidity. Absence of integrated joint sensors in manipulators that use piezoelectric stick-slip actuators (which is typical), as well as difficulty in using vision feedback for closed-loop control, has led to development of open-loop modeling methods to estimate the step size of the actuators. Prior work has failed to characterize and quantify the effects of various parameters on the displacement of such actuators to a degree as to be easily utilized in the control of an actual manipulator. In this thesis, we propose an empirically derived predictive open-loop model for the step size of the prismatic and rotary piezoelectric-stick-slip-actuated joints of a Kleindiek MM3A micromanipulator, based on static and inertial loads due to the mass of the manipulator's links as well as loads applied to the end-effector. The effects of various parameters on the step size of each joint are quantified and characterized. The results obtained are then fit into a model based on nonlinear regression via joint-specific parameters. Calibration routines are developed to quickly determine the joint-specific parameters for use in the derived predictive step-size model. Using the model obtained, we can predict the step size with an accuracy of 20% (100 nm) for the prismatic joint of the manipulator, and 2% (1 μrad) for the rotary joints of the manipulator.

CONTENTS

LIST OF FIGURES

ACKNOWLEDGMENTS

First, I would like to thank my advisor Dr. Jake Abbott for his utmost guidance and support as well as mentoring throughout the development of this project. I would also like to thank Manikantan Nambi for his contribution to the project as we have worked together throughout the development of this project. Finally, I would like to thank my family and friends who supported me and helped keep me motivated.

CHAPTER 1

INTRODUCTION

The need for precise micro/nano-positioning has arisen in many fields of research and technology, such as in the field of microbiology, electro-discharge machining, nanomaterial testing (e.g., carbon nanotubes), lithography, microelectromechanical systems (MEMS), and nanoelectromechanical systems (NEMS). The process of precise positioning at very high resolutions (to the scale of nanometers) can be implemented using effective and accurate positioning techniques. For the purposes of precise positioning at high resolution, while still allowing significantly larger range of travel, concepts such as stick-slip motion, impact drive principle, and inchworm-type motion have been employed by many researchers [1–3], with hydraulic, piezoelectric, pneumatic, and moving-coil actuators being the most common types of actuators that have been used for precise positioning. The stick-slip devices are characterized by a comparatively simple design consisting of few parts, backlash-free motion, and very high resolution. This makes them attractive for building up small, cheap, and accurate positioners. The piezoelectric actuator is based on the piezoelectric effect, wherein application of a voltage to the material causes it to expand. The result is very high voltages corresponding to only tiny expansion of the piezoelectric material. Moreover, they have a very high power-to-weight ratio, and therefore, can be scaled down and made compact. When these piezoelectric actuators run on the concept of stick-slip motion, they are termed "piezoelectric stick-slip actuators." Piezoelectric stick-slip actuators have a simple structure, high positional accuracy owing to their small piezoelectric coefficient [4], and theoretically unlimited distance [5, 6]. In addition, they have high stability and stiffness as they are supported by guiding surfaces [7]. Due to the above reasons, piezoelectric stick-slip actuators have proven to be very useful for achieving submicron accuracy and very fast response. Thus, these devices have been incorporated into many micropositioners and have drawn extensive attention over the last decade.

The piezoelectric stick-slip actuators work on the principle as shown in Fig. 1.1. The actuator consists of a piezoelectric element and a sliding mass that moves relative to the
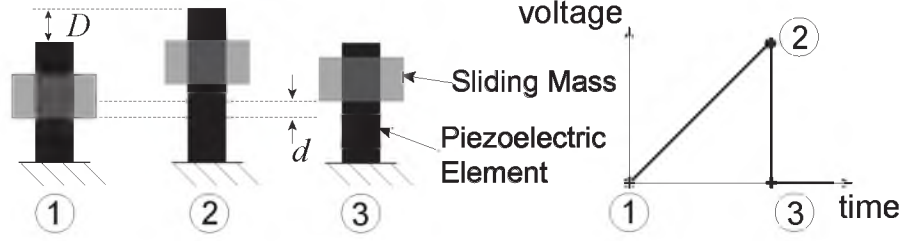
Figure 1.1. Working principle of a piezoelectric stick-slip actuator. As the voltage slowly increases from 1 to 2, the piezoelectric element stretches by a distance D, and due to stick-slip friction between the piezoelectric element and the sliding mass, the sliding mass also advances. When the voltage is quickly reduced from 2 to 3, the piezoelectric element quickly shrinks, but the inertia of the sliding mass prohibits it from moving backward as quickly, resulting in a net forward displacement of the sliding mass of $d < D$.

piezoelectric element. The sliding mass is attached to the piezoelectric element via friction [8]. A sawtooth voltage signal is applied to the piezoelectric element. As the voltage slowly increases from point 1 to 2, the piezoelectric element expands. The friction between the piezoelectric element and the sliding mass causes the mass to move with the expanding element. This is called the "stick" phase. Then, the voltage is quickly reversed from 2 to 3 leading to the piezoelectric element being retracted very quickly in the opposite direction. This, in turn, leads to the mass sliding relative to the piezoelectric element because the force due to inertia becomes larger than the friction between the piezoelectric element and the sliding mass. This is called the "slip" phase. By alternating between the stick and slip phase, infinite motion in either direction is possible. Movement can occur in two phases, namely the fine mode (used for achieving the highest resolution possible) and the coarse mode (used for taking comparatively larger discrete steps and for achieving quicker motion).

In recent years, several companies such as Physik Instrumente [9], NanoControl [10], and Nanomotion [11] have developed innovative piezoelectric-based actuators for the purposes of precise positioning at the micrometer and nanometer scale. More products based on inertial drives or walking mechanisms have now become available (e.g., SmartAct and Piezomotor) [12, 13]. The Kleindiek MM3A ([14], Fig. 1.2), the Zyvex Nanomanipulator [15], Imina Technologies miBot [16], and the Attocube Nanopositioners [17] are some of the commercial manipulators based on piezoelectric stick-slip actuators.

One major challenge in the field of micromanipulation is controlling piezoelectric stick-slip actuators, as these actuators have a discrete step nature. Hence, it is not possible to send a continuous signal to these actuators to achieve continuous motion for the end-effector
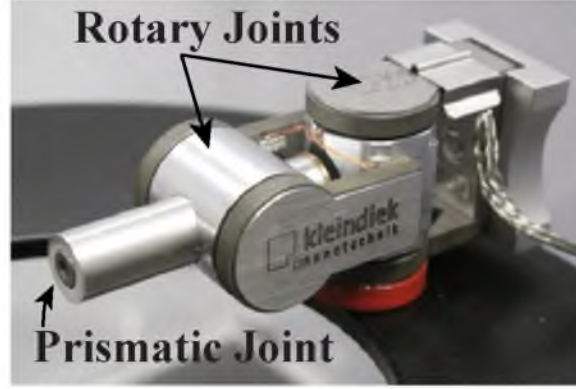
Figure 1.2. The Kleindiek MM3A micromanipulator, manufactured by Kleindiek Nanotechnik, is a RRP manipulator that utilizes piezoelectric stick-slip actuators. This is the manipulator used throughout this thesis.

mounted on the manipulator. The input must be given in the form of number of steps to be taken by each joint of the manipulator. The problem is that these stick-slip actuators, being intimately connected with friction and inertia, do not have fixed step sizes, but rather, the step sizes vary based on the external loads on the nanomanipulator [18], the mass of the manipulator's links, environmental conditions [19, 20], and various other factors [21]. Moreover, such devices typically lack sensor feedback, making it difficult to control the system's behavior in a closed-loop fashion.

To accurately control micro/nano-manipulators with piezoelectric stick-slip actuators, various closed-loop control schemes, typically using a vision system, have been implemented. Saiedpourazar and Jalili [22,23] developed an adaptive controller to estimate the parameters of the manipulator, and fused visual servoing and force feedback to enable closed-loop automatic control of the Kleindiek MM3A. Yang et al. [24] developed a closed-loop controller for micromanipulation in an atomic force microscope (AFM). A multitude of other feedback-control schemes such as voltage/frequency control [25], hybrid control [26], and sliding-mode control [27] have been implemented. Research utilizing vision feedback from the scanning electron microscope (SEM) [28] and optical microscope [29] images has also been done. However, closed-loop control of manipulators using imaging data is challenging as real-time nanoscale visual and force data is difficult to obtain [30]; such closed-loop techniques also require a dedicated SEM, which is not available to all researchers.

In addition to friction, the behavior of piezoelectric systems are predominantly affected by nonlinearities such as hysteresis, creep, and drift [31], which degrade their performance. Due to the presence of such nonlinearities, it becomes necessary for accurate modeling of

the dynamics for the displacement of these piezoelectric stick-slip actuators. This includes modeling of the nonlinearities including friction and hyteresis as well as modeling the piezoelectric element.

The research group at EPFL in Switzerland [1, 2] has focused their research on these actuators for precise manipulation and nanoscale motion control. They have designed, developed, and modeled various manipulators and microrobots based on piezoelectric stick-slip devices. Edeler and Fatikow [4, 32] at University of Oldenburg in Germany have developed techniques for open-loop control of piezo-actuated systems. Lockwood et al. [33] characterized the performance of these actuators against gravity, and Peng and Chen [18] shed light on the effect of the end-effector mass on the behavior of such systems. Many other models (discussed in Chapter 2) utilizing different techniques for modeling piezo-actuated systems have been developed. However, knowledge of the effect of static and dynamic parameters on the behavior of piezoelectric stick-slip systems is still lacking in literature. In addition, there has been no attempt to accurately model the behavior of the piezoelectric stick-slip motion in its coarse mode.

The goal of this thesis is to quantify the effect of loads on the behavior of these piezoelectric stick-slip actuators being driven in coarse mode. By doing so, we take a first step toward accurate control of micro/nano-manipulators with piezoelectric stick-slip actuators. Specifically, we will (1) experimentally demonstrate the effect of various static loading conditions on the step size of the rotary and prismatic joints of the Kleindiek MM3A manipulator, (2) develop analytical predictive models, based on empirical data, for the effect on the joints of the MM3A based on current loading conditions, and (3) develop calibration routines to quickly determine joint-specific parameters for use in the derived predictive step-size model. With this approach, we propose to accurately control the motion of micro/nano-manipulators by utilizing the derived empirical model in algorithms such as the one we presented in [34], which converts desired manipulator end-point commands into the appropriate number of commanded joint steps.

In Chapter 2, an introduction to the Kleindiek MM3A [14] and a review of existing literature on modeling of piezoelectric stick-slip actuators is discussed. The kinematics and dynamics of the MM3A (modeled as a traditional robotic manipulator) are presented in Chapter 3, and the effects of related static and dynamic parameters are discussed. An empirical model describing the effect of static loads on prismatic joints of the MM3A is developed in Chapter 4. An empirical model describing the effect of static loads and inertial load due to link 3 on rotary joint of the MM3A is developed in Chapter 5. A calibration

routine to determine the free model parameters is discussed in Chapter 6. Finally, the conclusion and potential future work is presented in Chapter 7. The full development of the forward and inverse kinematics, manipulator Jacobian, and Lagrangian dynamics of the MM3A is given as an appendix.

CHAPTER 2

BACKGROUND

Modeling of piezoelectric stick-slip actuators is a challenging task. This is mainly due to the nonlinear nature of friction and hysteresis, which significantly affects the behavior of these actuators [31]. Consequently, a number of studies have focused on modeling these nonlinearities in a model of piezoelectric actuators. Moreover, when dealing with micromanipulation, various other factors such as pre-sliding displacement [35,36] and environmental conditions have been shown to significantly affect the performance of these actuators. The working principle of the piezoelectric stick-slip actuator is explained in Chapter 1. In this section, we will give an overview on the characteristics of the Kleindiek MM3A. We will also discuss some of the dynamic models of these actuators presented by different research studies. Various studies have been conducted that shed light on the effect of certain external and intrinsic factors on the performance of these actuators. We conclude this chapter by summarizing the work of previous studies and comparing it with our work.

2.1 The Kleindiek MM3A Micromanipulator

The Kleindeik MM3A micromanipulator is a three-degree-of-freedom (3-DOF) rotary-rotary-prismatic) (RRP) manipulator. It consists of three piezoelectric-driven actuators, named Nanomotors®, based on the same principle as described in Fig. 1.1. The two modes of movement (coarse and fine), which are described in section Chapter 1, are shown in Fig. 2.1. The piezoelectric actuators utilized in the MM3A provide wide range of motion ($240°$ in the revolute joints and 12 mm in the prismatic joint). Each step of the end-effector in fine mode corresponds to 5 nm due to revolute actuators and 0.25 nm due to prismatic actuators, and each step in coarse mode corresponds to $20\,\mu$m and $15\,\mu$m for joints 1 and 2 (revolute joints), respectively, and $1\,\mu$m due to joint 3 (prismatic joint) [6]. This nanoscale precision combined with a wide range of motion is achieved due to the stick-slip movement of the Nanomotors®. The amplitude of the applied voltage signal determines the step size, and the frequency of the signal affects the speed at which each step is executed.
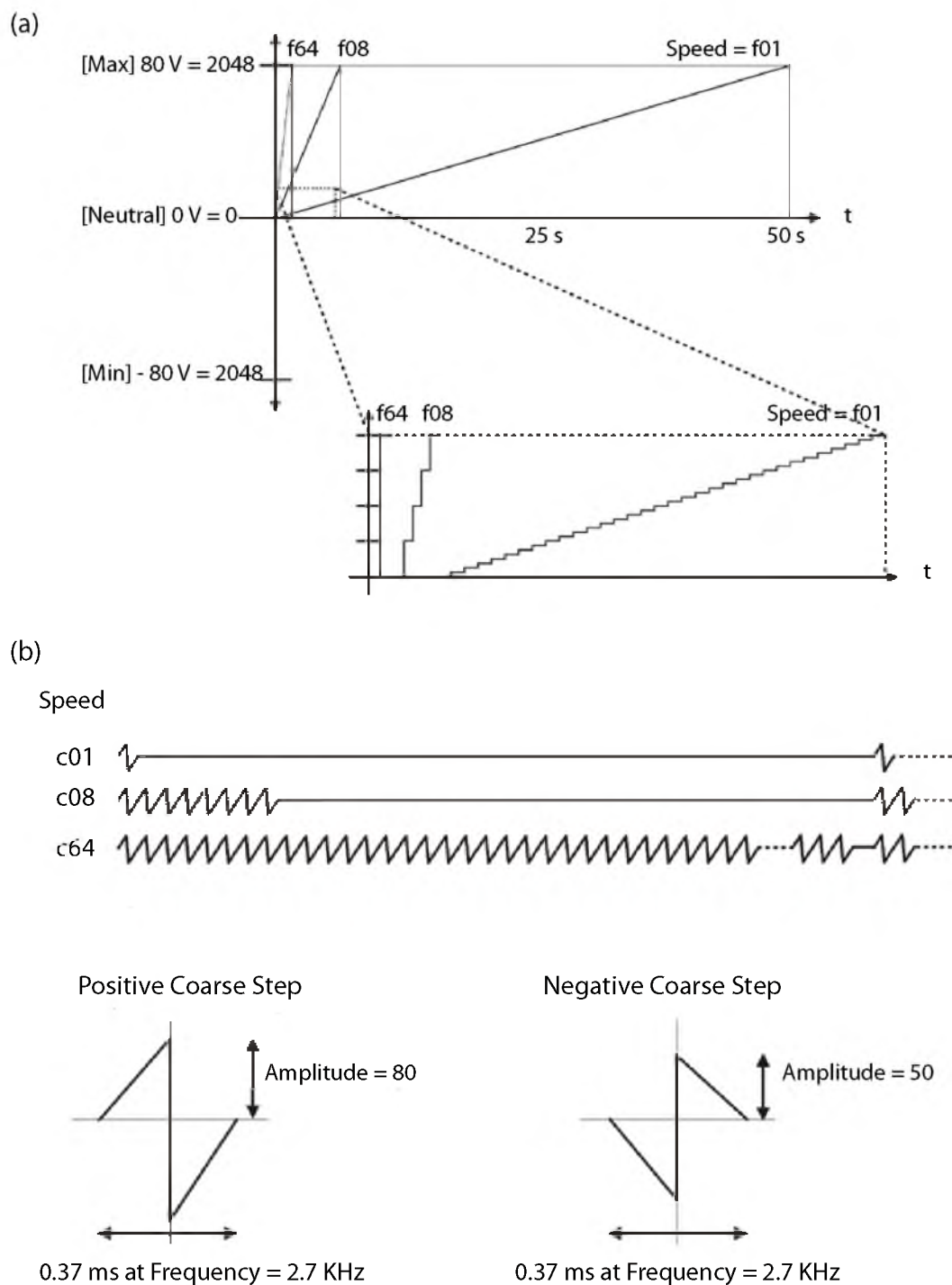
Figure 2.1. The Kleindiek MM3A micromanipulator's (a) fine positioning and (b) coarse positioning modes [6]. Reprinted with permission.

2.2 Prior Work in Modeling of Piezoelectric Stick-slip Actuators

In the modeling of piezoelectric stick-slip actuators, early remarkable work was contributed by Pohl [37]. In Pohl's study, the piezoelectric actuator was simplified as a simple linear component, and the relationship between displacement of the piezoelectric actuator and the driving voltage was represented using a linear function. The following equation governed the study:

$$\Delta X = D(\Delta V)$$
$$F_p = E(\Delta V)$$

where ΔX is the expanding displacement of piezoelectric actuator, F_p is the force generated by the piezoelectric element, ΔV is the voltage difference applied to the piezoelectric actuator, and E and D are coefficients relating the voltage to the force and the displacement, respectively. However, this model failed to take into account the friction nonlinearity as well as the piezoelectric element's dynamics. Rabinowicz [21] studied the effect of static and kinetic friction on the stick-slip system via different experiments, and concluded that they have a significant effect on its displacement.

In another study, Chang and Li [38] developed a model for a piezoelectric actuator with a programmable step size. The schematic diagram of their actuator model is shown in Fig. 2.2, in which M is the mass of the movable stage, m the mass of the slider or end-effector, k is the stiffness of the spring, and c is the damping of the damper. The equations for the motion of the slider resting horizontally on the movable platform are:

$$(M+m)\frac{d^2X}{dt^2} = -c\frac{dX}{dt} - k(X - \Delta L(t)) - (\mu mg)\text{sgn}\left(\frac{dX}{dt} - \frac{dx}{dt}\right)$$
$$m\frac{d^2x}{dt^2} = -(\mu mg)\text{sgn}\left(\frac{dx}{dt} - \frac{dX}{dt}\right)$$

In this work, the friction between the slider and the movable platform was represented by Coulomb friction. However, the friction observed in stick-slip piezoelectric actuators has been shown to have far more complex nature than just Coulomb friction [39–42].

Goldfarb et al. [43] developed a nonlinear lumped parameter model of a piezoelectric actuator. Their model, which consists of both mechanical and electrical domains, as well as the connection between the two domains, is shown in Fig. 2.3. Their model was based on the generalized Maxwell resistive capacitor to represent the static hysteresis that is observed in piezoelectric actuators. This was represented by a generalized elastoplastic Maxwell-slip model [44]. Despite the presence of this nonlinearity, the dynamics of the piezoelectric
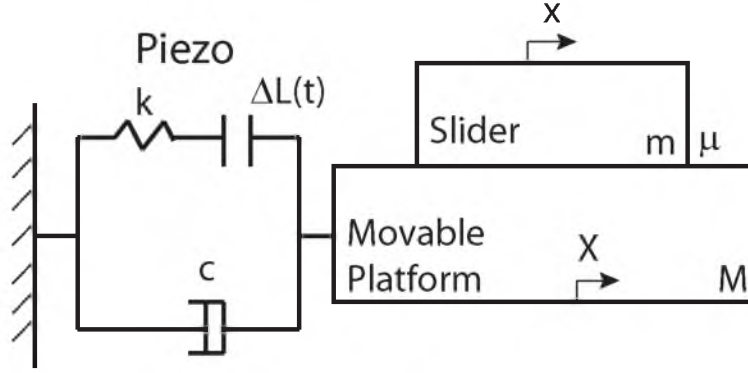
Figure 2.2. Simulation model of the piezoelectric-driven stick-slip actuator used by Chang and Li in [38]. Reprinted with permission.
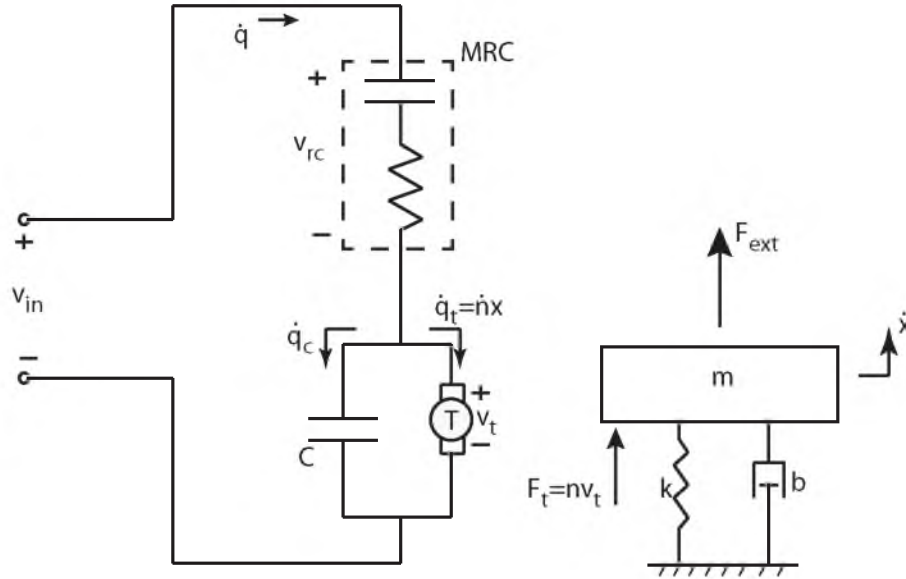
Figure 2.3. Electromechanical model used by Goldfarb [43]. Reprinted with permission.

actuator was observed to have simple second-order linear characteristics. Adriaens et al. [45] elaborated on the model presented by Goldfarb by incorporating a nonlinear first-order hysteresis effect and by modeling the piezoelectric actuator as a distributed parameter system. They studied the influence of the positioning mechanism on the overall behavior of the actuator based on the mechanical model of the actuator using Bode plots and root locus, and concluded that if the positioning system was designed well, the aforementioned second-order approximation was a good estimate of the system dynamics. The combination

of the piezoelectric element and slider mass was modeled as a simple mass-spring-damper system, and the interaction force between the piezoelectric elements and the slider mass, denoted by F_s, was given by:

$$m_s \ddot{y} + c_s \dot{y} + k_s \quad = \quad F_s$$

Chen et al. [46] modeled these piezoelectric stick-slip actuators as a second-order system and provided a rationale for this second-order approximation, by employing the assumed mode method to solve the governing equation. They provided the scope of and the errors involved with this approximation of the system dynamics.

Comprehensive simulations were presented by a group at EPFL, Switzerland. Breguet [47] designed several prototypes based on stick-slip actuators and designed an electromechanical model of the piezo-actuator, with the friction force at the mechanical interface being modeled by a simplified form of the LuGre model [42]. Bergander [48] applied this aforementioned model to devise a signal shaping technique to improve the behaviour of piezoelectric stick-slip dynamic system.

Zesch et al. [49] presented and analyzed two novel stick-slip mechanisms: Abalone and NanoCrab. Mathematical formulae are derived to calculate step size and control signal timing. They were found to have open-loop operation error of less than 1%. Their formulae, however, are based on parameters, which are not further investigated. Another study by Eigoli et al. [50] focused on developing a stick-slip model for a legged, piezoelectric-driven microrobot. Hamilton's principle, a linear piezoelectric relation, and linear Euler-Bernoulli beam theory was used to derive the system's equation of motion. The model is comprised of the motion of these actuators in terms of robot's physical characteristics, friction coefficient, and applied electrical voltage.

In recent years, only few research institutions worldwide dealt with piezoelectric stick-slip actuators as micropositioners; however, advancements have been made as far as understanding thier complexities are concerned. Studies have shown that for precise positioning at micro/nano-scale, more needs to be done in regards to characterizing the stick-slip nature of these actuators [32]. The phenomenon of pre-sliding, which has been found to have significant effect on the displacement of these stick-slip drives, has thus come under examination. Al-Bender et al. [35, 36] presented a comprehensive investigation into this phenomenon. Studies have shown that in minute motion, the friction in these actuators is dominated by pre-sliding displacement, and its nature is inherently different from Coulomb friction. This displacement affects the step size as it affects the friction in these actuators.

Peng et al. [18] developed a model for stick-slip actuators, incorporating pre-sliding effect into the elastoplastic LuGre model. They also presented the effect of change in end-effector mass on the performance of stick-slip actuators. The model used in [18] is:

$$M\ddot{x}_1(t) + C\dot{x}_1(t) + Kx_1(t) = Du(t)$$
$$Du(t) = H(t) - F_f$$

where $H(t)$ is the Hysteresis model and F_f is the friction model:

$$F_f = \sigma_o(M_e)z + \sigma_1\dot{z}$$
$$\dot{z} = \dot{x}[1 - \frac{\alpha(z)z}{\beta M_e/\sigma_o}]$$

where $\sigma_o(M_e)$ denotes that σ_o is a function of the end-effector mass (M_e). Fig. 2.4 shows the effect of end-effector mass on the performance of stick-slip actuators.

A consequent piecewise function for $\sigma_o(M_e)$ was formulated as follows:

$$\sigma_o(M_e) = -(5.07 \times 10^5)M_e^3 + (1.25 \times 10^5)M_e^2 + 287M_e + 90.8$$
$$= \text{when } M_e \leq 0.157$$
$$\sigma_o(M_e) = (4.71 \times 10^5)M_e^3 - (3.35 \times 10^5)M_e^2 + (7.22 \times 10^4)M_e - 3.66 \times 10^3$$
$$= \text{when } 0.157 < M_e \leq 0.253$$
$$\sigma_o(M_e) = -(2.29 \times 10^4)M_e^3 + (4.06 \times 10^4)M_e^2 - (2.29 \times 10^4)M_e^2 + 4.36 \times 10^3$$
$$= \text{when } M_e > 0.253$$

Fig. 2.4 shows that the end-effector speed increases with end-effector mass up to a certain value of mass, and then decreases with mass.

Edeler et al. [32] recently presented a comprehensive model of piezoelectric stick-slip actuators for micromanipulation. They further investigated the effect of normal contact force, the aspects of elastic deformation, and the concept of pre-sliding. These effects were incorporated into a modified elastoplastic model, the parameters of which were derived from the material properties, and an empirical model of the preload characteristics was presented.

Lockwood et al. [33] characterized the performance of slip-stick actuators against gravity. He found that the step size of these slip-stick motors was affected by gravitational forces by ±8%. However, he did not further model the behavior of these motors. Li et al. [51] investigated the thermal effect on these actuators and based on their experiments concluded that temperature change affects the displacement of the actuators. Moreover, their studies also showed the temperature changes within the system with time, leading to
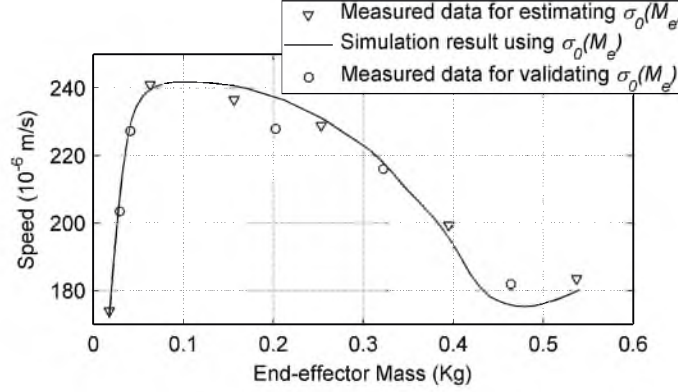
Figure 2.4. Measured and simulated results showing the effect of end-effector mass on stick-slip displacement [18]. Reprinted with permission.

a sense of thermal wear. They utilized their findings in the modeling of the piezoelectric stick-slip actuator by incorporating the thermal effects [52]. Another study by Cain et al. [53] concluded that the atmospheric relative humidity and temperature has a marked effect on the displacement of stick-slip actuators.

2.3   Summary and Comparison to the Current Work

It is clear that a great deal of research has been conducted on the modeling and performance characterization of piezoelectric stick-slip actuators for micropositioning. Different techniques for modeling these actuators, ranging from modifying friction or hysteresis models to studying the effect of environmental conditions and change of parameters, have been used. In all of the prior literature, however, the effects of parameters such as inertia, gravity, and forces applied to the manipulator's end-effector on these stick-slip actuators have not been quantified in a way that can used to predict the step size of an actuator as a function of the current configuration and applied loads of the manipulator. In this thesis, we present a novel approach to quantifying the effects of static (i.e., noninertial) loads on the step size of these actuators, as a starting point for our larger modeling goals. A mathematical model is formed that is based on empirical data that does not require a sophisticated physics-based model, and must simply be calibrated using a set of well-defined controlled motions of the manipulator's joints. This empirical model can be used for effective analytical prediction of the step size of the actuators.

CHAPTER 3

SIMPLIFIED DYNAMICS OF THE
KLEINDIEK MM3A

Derivation of the *dynamic model* of a manipulator plays an important role in simulation of motion, analysis of manipulator structures, and design of control algorithms. Computation of the forces and torques required for the execution of typical motions provides useful information regarding the manipulator parameters. The dynamic equations explicitly describe the relationship between force and motion [54].

The main goal of this study is to analyze the effect of various dynamic parameters such as inertial, gravitational, and Coriolis terms on the manipulator joints considering the fact that each joint step begins and ends with the manipulator at rest, due to the discrete-step nature of the piezoelectric stick-slip actuators. In this chapter, we show the dynamic equations of the manipulator, which are simplified based on our discrete-stepping assumption; we show that the forces and torques acting on the Kleindiek MM3A depend only on the diagonal elements of the inertial matrix and on the gravitational effects.

Kinematically, the Kleindiek MM3A manipulator is no different than any traditional robotic manipulator in the sense that that each joint of the manipulator results in the movement of the end effector (Fig. 3.1). Fig. 3.2 shows the parameterization of the manipulator as per D-H convention.

Moreover, we can relate these joint movements to end-effector movement via a configuration dependent manipulator Jacobian, $J(\vec{\theta})$ such that

$$\dot{\vec{X}} \;=\; J(\vec{q})\dot{\vec{q}} \tag{3.1}$$

where $\vec{q} = [q_1 \quad q_2 \quad q_3]^T$ is the vector of joint positions, $\vec{X}$ is the position of the end effector, and the "dot" indicates a time derivative.

Dynamically, a serial-link nanomanipulator has the same governing dynamic equation as a traditional robotic manipulator:

$$M(\vec{q})\ddot{\vec{q}} + C(\vec{q},\dot{\vec{q}})\dot{\vec{q}} + G(\vec{q}) - J^T(\vec{q})\vec{f} \;=\; \vec{\tau} \tag{3.2}$$

Figure 3.1. The Kleindiek MM3A (RRP) manipulator.
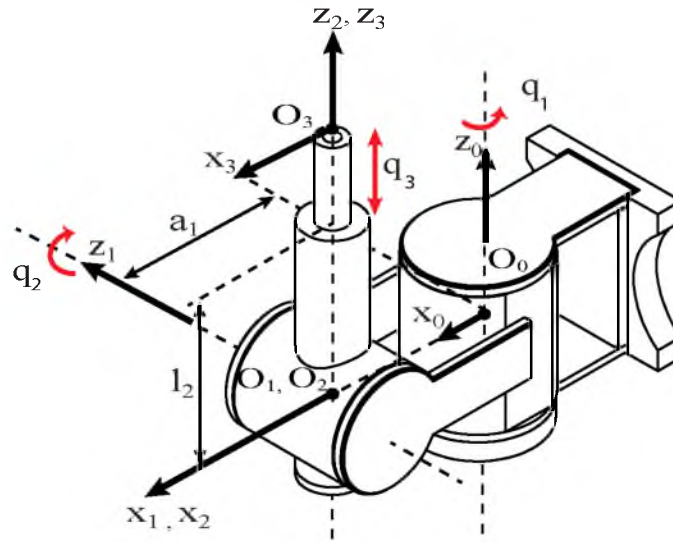
Figure 3.2. The Kleindiek MM3A (RRP) manipulator with D-H parameters at its zero angle position.

where $M(\vec{q})$, $C(\vec{q}, \dot{\vec{q}})$, and $G(\vec{q})$ are configuration-dependent inertia, Coriolis, and gravity matrices, respectively. $\vec{f}$ is any load applied to the tip, and $\vec{\tau}$ is the vector of actuator torques and forces. This equation is useful for control of traditional robotic manipulators, where we have direct control over the joint torques and forces. However, in the case of a manipulator such as the Kleindiek MM3A, torques/forces cannot be directly controlled at each joint due to the discrete nature of the piezoelectric stick-slip actuators. Rather,

discrete steps must be commanded. Moreover, each discrete joint step begins and ends with the manipulator at rest. However, (3.2) is still a valid equation, and matrices $M(\vec{q})$, $C(\vec{q}, \dot{\vec{q}})$, and $G(\vec{q})$ are still valid. Knowledge of how these matrices affect the end-effector movement during each discrete step will help in accurate control of the manipulator.

The full dynamics of Eq. 3.2 for the Kleindiek MM3A are derived in appendix A, along with the derivation of the forward and inverse kinematics and the manipulator Jacobian. The dynamics are derived there under the assumption that the actuators provide general torque/force, such as would be the case with the DC motors of a traditional manipulator. Here, we present the simplified dynamic equations that result for the discrete-step nature of the joints. Because the joints are stepped one at a time, when joint 1 is moving, $\dot{q}_1 \neq 0$ and $\ddot{q}_1 \neq 0$, but $\dot{q}_2 = \ddot{q}_2 = \dot{q}_3 = \ddot{q}_3 = 0$. The relationships of joints 2 and 3 are analogously defined. The results is a significantly simplified dynamic equation that can be used during the coarse stepping mode:

$$\begin{bmatrix} M_{11}\ddot{q}_1 \\ M_{22}\ddot{q}_2 \\ M_{33}\ddot{q}_3 \end{bmatrix} + \begin{bmatrix} G_1 \\ G_2 \\ G_3 \end{bmatrix} - J^T(\vec{q})\vec{f} = \vec{\tau} \tag{3.3}$$

where

$$M_{11} = m_1 r_1^2 + {}^0I_{133} + {}^0I_{233} + {}^0I_{333} + m_2(a_1 - r_2 s_2)^2$$
$$+ m_3(a_1 - (l_2 + q_3 - r_3)s_2)^2 \tag{3.4}$$

$$M_{22} = m_2 r_2^2 + s_1^2({}^0I_{311} + {}^0I_{211}) + c_1^2({}^0I_{322} + {}^0I_{222}) - s_1 c_1({}^0I_{321}$$
$$+ {}^0I_{312} + {}^0I_{221} + {}^0I_{212}) + m_3(l_2 + q_3 - r_3)^2 \tag{3.5}$$

$$M_{33} = m_3 \tag{3.6}$$

and

$$G_1 = m_1 r_1 g_1 s_1 - m_1 r_1 g_2 c_1 + m_2 g_1(a_1 s_1 - r_2 s_1 s_2) - m_2 g_2(a_1 c_1 - r_2 c_1 s_2)$$
$$+ m_3 g_1(a_1 s_1 - (l_2 + q_3 - r_3)s_1 s_2) - m_3 g_2(a_1 c_1 - (l_2 + q_3 - r_3)c_1 s_2) \tag{3.7}$$

$$G_2 = m_2 r_2 g_1 c_1 c_2 + m_2 r_2 g_2 s_1 c_2 + m_2 g_3 r_2 s_2$$
$$+ m_3(l_2 + q_3 - r_3)g_1 c_1 c_2 + m_3(l_2 + q_3 - r_3)g_2 s_1 c_2$$
$$+ m_3 g_3(l_2 + q_3 - r_3)s_2 \tag{3.8}$$

$$G_3 = m_3 g_1 c_1 s_2 + m_3 g_2 s_1 s_2 - m_3 g_3 c_2 \tag{3.9}$$

The individual entries are defined in the appendix.

As can be seen in Eq. 3.3, the Coriolis terms of Eq. 3.2 have effectively become zero, and the joint forces and torques depend only on the gravitational terms and the diagonal

elements of the inertia matrix, due to the stepping of an individual joint. Forces applied to the end-effector pass through the Jacobian to load the joints, and the joints are unable to distinguish static loads due to applied forces from static loads due to gravitational terms. In this thesis, we consider the effect of gravitational loading on the joints, with an understanding that the results generalize to all static loads. We see that inertial loads on the rotary joints (M_{11} and M_{22}) can change as a function of the manipulator's configuration $\vec{q}$, so in this thesis we study inertial effects on the rotary joints. We see that M_{33} does not change with manipulator configuration, so we do not consider inertial effects on the prismatic joint; the effect of M_{33} is accounted for during calibration.

CHAPTER 4

EMPIRICAL MODEL OF THE
PRISMATIC JOINT

The step size of the prismatic joint is a function of the static loads acting on the actuator. This has been observed by a number of researchers as stated in Chapter 2, but never characterized and quantified. In this chapter, we study the effect of static loads on a prismatic piezoelectric stick-slip actuator using the distal prismatic joint of the Kleindiek MM3A, and we propose an analytical model to predict the step size of the prismatic joint γ_3 based on its current configuration. This model is based on empirical data collected from a finite set of experiments. Also, the effect of factors such as the normal force (the force between the slider and the stator), the configuration of the rotary joint 2, and change in environmental conditions that affect the step size of the prismatic joint are studied, and statistical tests are performed to test the significance of these factors on the step size.

4.1   Methods

In this section, we will discuss the methodology adopted to carry out experiments and generate the required results.

4.1.1   Euler Convention

Fig. 4.1 shows the D-H coordinates for the Kleindiek MM3A. Euler angles, as shown in Fig. 4.2, are used to describe the orientation of the manipulator base frame 0 in space. Coordinate system O_0 is the coordinate frame for the joint axis of joint 1, and the Euler angles θ and ψ are described as:

(1) θ is the angle made by rotating the manipulator about an original world frame's x_0. In other words, it is the angle between the world's vertical z_0 with the new local z_0' as shown in Fig. 4.2(c).

(2) ψ is the angle made by rotating the manipulator about the new local y_0'. It is the angle made by the previous local z_0' with the new local z_0'' as shown in Fig. 4.2(c).
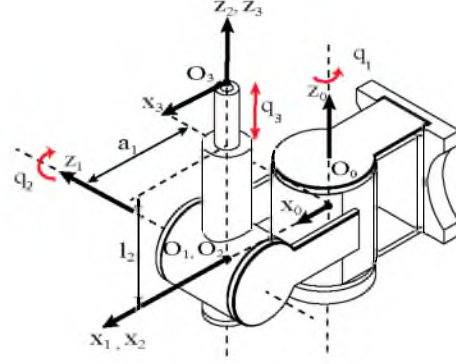
Figure 4.1. The Kleindiek MM3A (RRP) manipulator with D-H parameters at zero angle position.
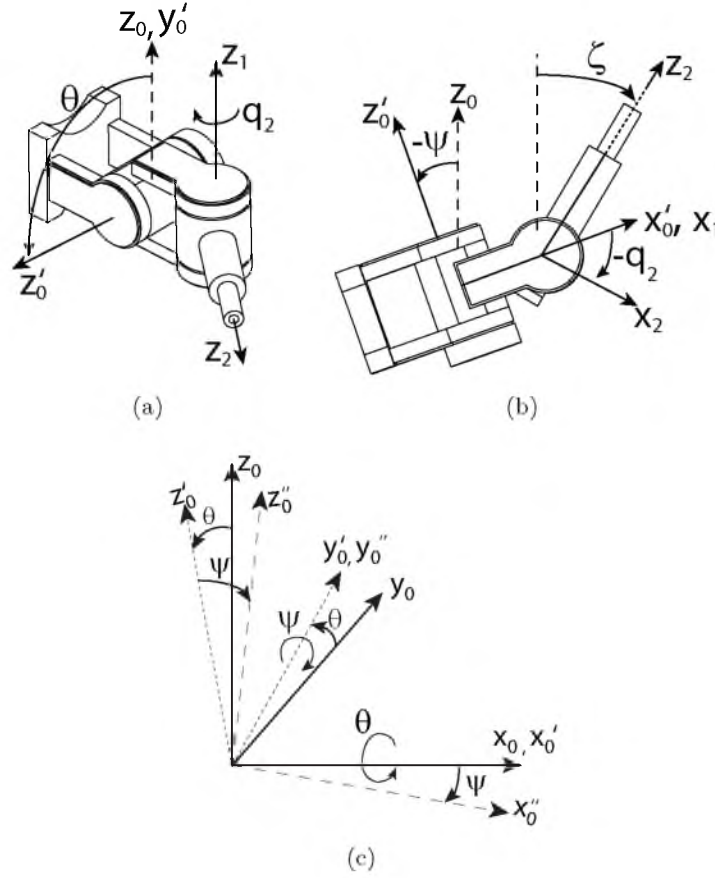
Figure 4.2. Kleindiek MM3A. With the z_0 axis initially vertical, the base frame is rotated by θ about x_0 and then rotated by ψ about y_0'. (a) Isometric view at $\theta = -\pi/2$. No gravitational loads acting on Joints 2 or 3. (b) Side view at $\theta = 0$, with gravitational loads acting on both Joints 2 and 3. $\zeta = \psi\text{-}q_2$. (c) The euler convention for describing the orientation of the Kleindiek MM3A.

(3) $\zeta = \psi - q_2$. In Fig. 4.2(b), ζ is shown to be equal to $-q_2$ as $\psi = 0$.

The orientation of the manipulator base frame with respect to the world frame is described by the rotation matrix $R = R_x(\theta)R_y(\psi)$.

4.1.2 Apparatus

The Kleindiek MM3A micromanipulation system consists of the MM3A micromanipulator and a NanoControl (NC) unit as shown in Fig. 4.3(a). The NC unit is used to command control signals to the manipulator. It has four knobs, three of which are used for controlling the three joints of the manipulator in fine and coarse mode. The number of steps to be taken by any particular joint corresponding to one turn of the knob can be set in the NC unit. In our experiments, the commands are being sent to this NC unit via a serial port. The time for one step was fixed at 10 ms and only one pulse per step was sent.

Before the start of any experiment, the joint is driven through its full range back and forth twice. This is done in an attempt to mitigate any transients in the data due to heating of the piezoelectric actuators; this effect has been explained in [51].

The step size of the prismatic joint is denoted by γ_3. As the step size of the prismatic joint is very small (on the order of $1\,\mu$m), it is not possible to visually detect when the joint reaches its end of travel. It was observed that a change in the sound of the piezomotor occurs upon hitting a mechanical stop. A custom software was made that monitors the sound from a microphone at each instant and computes the Fast Fourier Transform (FFT) of the audio signal. The sound when the joint hits a mechanical stop is detected as a peak in the power of the FFT. This FFT algorithm loops after every 5 steps, so the accuracy with which this system captures the end of travel is up to five steps, or within 0.005% of the actual steps taken to reach the end of travel. The frequency at which this peak occurs, and

(a) (b) (c)
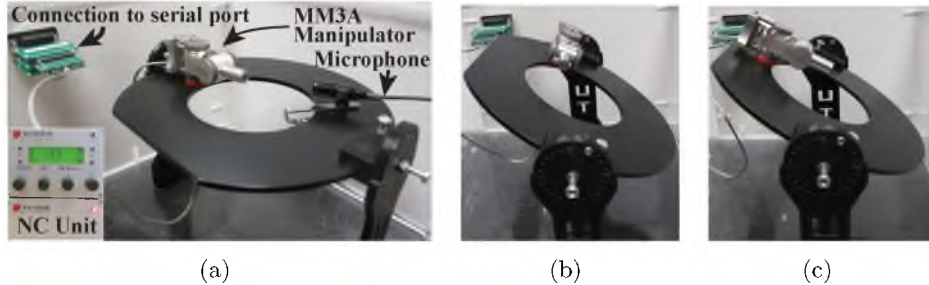
Figure 4.3. The Kleindiek MM3A manipulator is shown at different orientations. (a) $q_2 = -\pi/2$, $\theta = 0$, and $\psi = 0$; (b) $q_2 = -\pi/2$ and $\psi = 0$ at a particular θ; (c) $q_2 = -\pi/2$ and $\theta = 0$ at a particular ψ.

the intensity of the peak, may be different on different days, and thus, it has to be tuned before each experiment.

The general formula used for computing the average step size of joint j in direction i, $\overline{\gamma}_{ji}$, is

$$\overline{\gamma}_{ji} \;=\; \frac{R_j}{N_{ji}} \tag{4.1}$$

where R_j is the total range of joint j, N_{ji} is the number of steps taken across the range of motion, and $i \in \{+, -\}$ indicates the direction of joint motion. The number of steps (N_{3i}) the manipulator took while traversing the whole range was recorded and the average step size taken by the prismatic joint, $\overline{\gamma}_{3i}$, was computed by the following relation:

$$\overline{\gamma}_{3i} \;=\; \frac{12000000}{N_{3i}} \quad \text{nm} \tag{4.2}$$

The static load on the prismatic joint can be varied by changing the angles q_2, θ, and ψ. q_2 is changed by actuating joint 2. For changing θ and ψ, a fixture is used as shown in Fig. 4.3, which allows us to set the base plate at desired angles in steps of $15°$. Thus, different orientations of link 3 can be achieved by varying q_2, θ, and ψ as shown in Fig. 4.3.

4.2 Effect of Unmodeled Environmental Factors

Environmental conditions (e.g., temperature, humidity) are uncontrolled in our experiments, so there is no accurate model incorporating these factors. To minimize these unmodeled effects on the open-loop control of the Kleindiek MM3A, we propose to calibrate the joints before each session of use. This assumes that there is a significant change from day to day that warrants such recalibration. To substantiate this claim, the step size for prismatic joint 3 in the positive (γ_{3+}) and negative (γ_{3-}) direction were taken on two different days, which would incorporate the change in environmental conditions.

Fig. 4.4 shows the change in the step size of the prismatic joint over two different days. The configuration of the prismatic joint in this plot is kept constant (at $q_2 = -\pi/2$, $\theta = 0$, and $\psi = 0$) on both days, and three readings each of the step size value in both directions are taken on a single day. An ANOVA test on the data shows that the difference in step size on different days is statistically significant ($p < 0.05$) for both positive ($p = 0.0003$) and negative ($p = 0.001$) directions. The ANOVA test also shows a significant difference ($p = 0.000004$) in the step size between the positive and negative directions within a given day. Thus, calibration on the rotary joints is recommended each time the manipulator is to be used, and different calibration parameters should be found for each direction of motion.
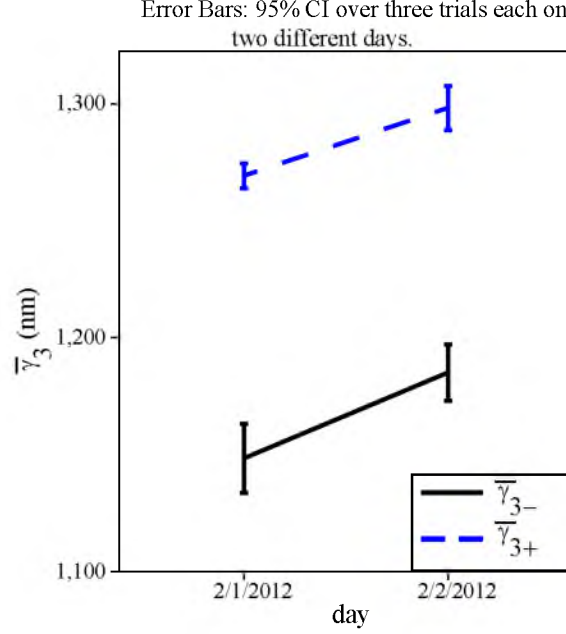
Figure 4.4. Plot showing the change in step size, $\overline{\gamma}_{3i}$ over two different days. The configuration of the manipulator was set at $q_2 = -\pi/2$, $\theta = 0$, and $\psi = 0$.

4.3 Experimental Procedure

We will now describe the experiments performed to analyze the effects of static loads on the prismatic joint. The procedures explained encompass the experiments for analysing the effect of joint angle q_2 combined with the effect of static loads, details of which will be explained in the subsequent sections. Step size γ_3 was recorded for values of q_2 ranging from 0 to $-\pi$ at fixed intervals of $-\pi/6$, at values of θ ranging from 0 to $-\pi/2$ at fixed intervals of $-\pi/6$, and at values of ψ ranging from $-\pi/2$ to $\pi/2$ at fixed intervals of $\pi/6$. The step size of joint 3 in the positive and negative directions is denoted by γ_{3+} and γ_{3-}, respectively. For each configuration of q_2, θ, and ψ, γ_{3+} was first recorded followed by γ_{3-}. The step size, $\overline{\gamma}_3$, was recorded in the following order to reduce drift in the data (if present):

(1) First, the MM3A was set at some angle ψ keeping $q_2 = -\pi/2$ and $\theta = 0$. The prismatic joint is first driven from $q_3 = 0$ to 12 mm in the positive direction and the average step size reading $\overline{\gamma}_{3+}$ is computed. Then, the joint is driven back (12 to 0 mm) to carry out its motion in the negative direction and the average step size reading $\overline{\gamma}_{3-}$ is computed. ζ, in this configuration, is equal to $\psi + \pi/2$.

(2) Next, the MM3A was fixed at $\theta = 0$ and $\psi = 0$. Joint 2 was set at some angle q_2. $\overline{\gamma}_{3+}$ and $\overline{\gamma}_{3-}$ were recorded in the manner described above. ζ, in this case, is equal to $-q_2$.

(3) Next, the MM3A was titled at angle θ, keeping the same value of q_2 used in the

above step, with $\psi = 0$. The step size in both directions was then recorded for the entire range of θ at fixed intervals as mentioned before.

(4) Steps 1 to 3 are repeated at the increments of ψ and then q_2 at their fixed intervals within their aforementioned range.

The recordings for the step size for the prismatic joint at configurations of $\psi = 0$ and $q_2 = -\pi/2$ at values of θ ranging from 0 to $-\pi/2$ at fixed intervals of $-\pi/6$ are used to analyze the effect of normal force on the prismatic joint. The analysis for this is explained in Section 4.4. The step size recordings gathered at $\theta = -\pi/2$ at fixed intervals of q_2 in the range 0 to $-\pi$ and at $\psi = 0$ was used to study the step size of the prismatic joint with no gravitational force acting on it. The analysis of this is explained in Section 4.5. The orientation of the manipulator at fixed intervals of ψ, at fixed intervals of q_2 in the range 0 to $-\pi$, and at $\theta = 0$ allows us to isolate the effect of gravity acting on the prismatic joint and thus, the step size recordings we gather in this configuration was used to analyze the effect of gravity (and thus all static loads) on the joint. The analysis of this is explained in Section 4.6.

4.4   Effect of Normal Force between Slider and Stator

In the case of piezoelectric stick-slip actuators, the normal force is the force between the piezoelectric element and the sliding mass. The force of friction is dependent on this force, and the fact that friction has an effect on the step size of the actuator is evident from the review of Chapter 2. Although the third link of the MM3A appears radially symmetric, in this section we verify that the step size is unaffected by rotations about the axis of the prismatic joint.

Fig. 4.5 shows configurations of the manipulator at which $\overline{\gamma}_{3-}$ and $\overline{\gamma}_{3+}$ recorded were used to obtain Fig. 4.6. Fig. 4.6 shows that changing θ does not seem to affect $\overline{\gamma}_{3i}$. An ANOVA test was performed on the data of the step size in the positive and negative directions, which revealed that the rotation of the prismatic joint about its axis is insignificant in both the positive ($p = 0.4$) and negative ($p = 0.9$) directions of the prismatic joint. Thus, the need for incorporating this effect in the modeling of the step size of joint 3 is eliminated.

4.5   Effect of Joint Angle q_2

Fig. 4.7 shows the orientation of the Kleindiek MM3A for the experiments to study the effect of joint angle q_2 on the step size of the prismatic joint, independent of static loads. One might expect the step size of joint 3 in this configuration to be a constant as there is
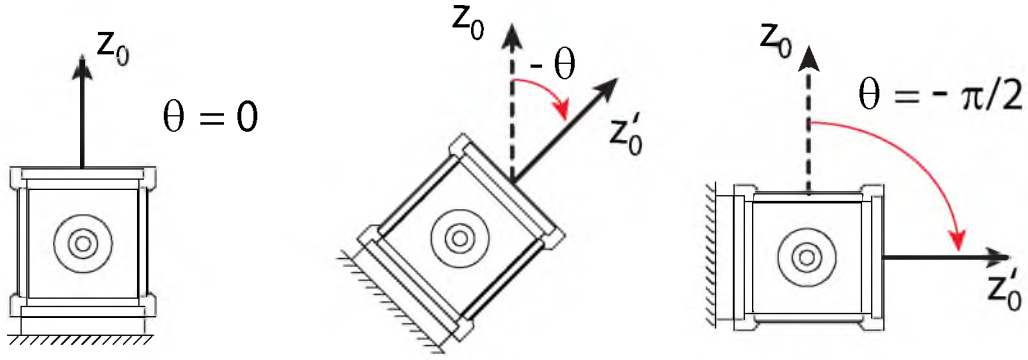
Figure 4.5. Procedure of experiment for analyzing the effect of normal force between the stator and the slider on joint 3. The figure shows the front view of the outstretched manipulator.
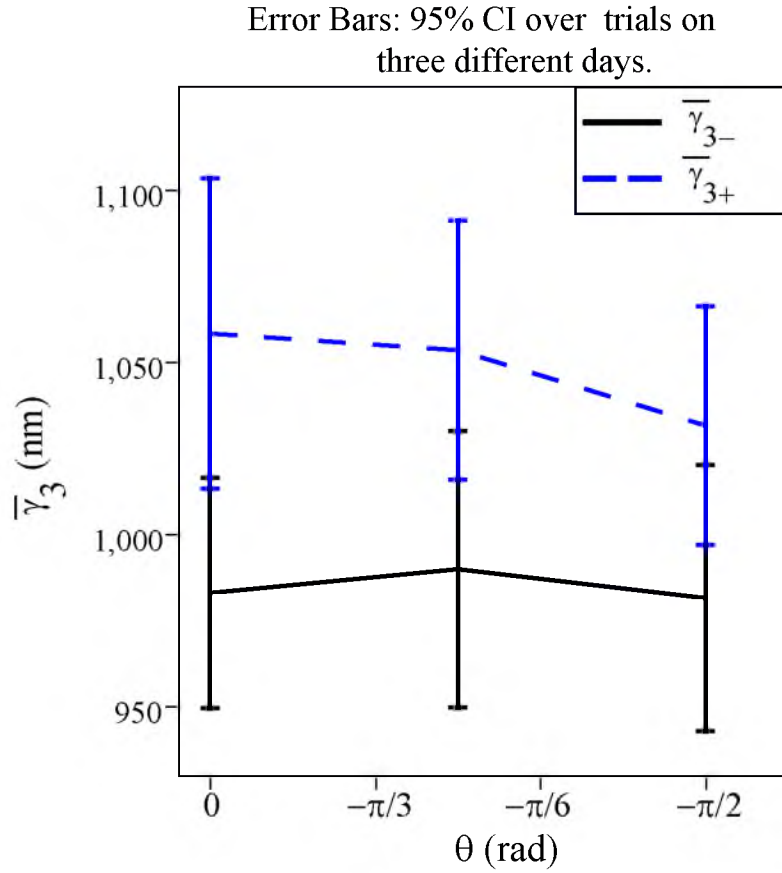
Figure 4.6. Plot showing the effect of normal force on change in step size $\overline{\gamma}_{3i}$ at $q_2 = -\pi/2$, $\psi = 0$, and at fixed intervals of θ.
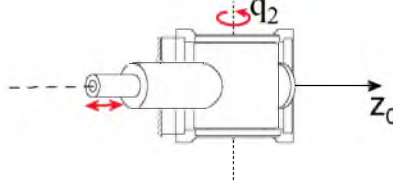
Figure 4.7. Figure showing orientation of the manipulator (at $\theta = -\pi/2$ and $\psi = 0$) for conducting the experiment for analyzing the effect of joint angle q_2.

no effect of gravity acting on the link. The results of the experiment are shown in Fig. 4.8. In Fig. 4.8(a), we see that $\overline{\gamma}_{3i}$ is not constant, rather, it changes with the joint angle q_2. The result from Fig. 4.8(a) is normalized into Fig. 4.8(b) by dividing the step size, $\overline{\gamma}_{3i}$, at a given q_2 in the shown configuration by the step size achieved at q_2=-$\pi/2$. This gives us an efficiency factor, $\eta(q_2)$ that is a function of q_2, as shown by the equation below:

$$\eta(q_2) = 1 - b_i|\cos q_2| \tag{4.3}$$

where b_i is a dimensionless free parameter to be determined via calibration. This equation has a maximum efficiency at $q_2 = -\pi/2$. The reduced step size, $\overline{\gamma}_{3i}$, at different values of q_2 other than $-\pi/2$ is most likely due to the component of the recoil force of the actuator acting perpendicular to the link connecting joint 1 to joint 2, which causes a small deflection in the link (which is not infinitely rigid). This effect is captured by $b_i|\cos q_2|$. The free parameter, b_i, captures the loss of stepping efficiency when the prismatic joint is fully perpendicular to the maximum-efficiency configuration.

4.6   Effect of Static Loads

Fig. 4.9 shows the manipulator in three different configurations of ψ, with q_2 and θ fixed. It describes the sequence of the configuration of the manipulator at which γ_{3i} was recorded in order to analyze the effect of gravity on the step size of the joint. The experimental procedure for the same has been explained in Section 4.3. In order to isolate the effect of gravity without any loss in the stepping efficiency, θ and q_2 are kept constant as shown in Fig. 4.9. Fig. 4.10 shows the effect at $\theta = 0$, while γ_{3i} is a constant for $\theta = -\pi/2$. The behavior of the system with respect to the change in gravitational force seems to be well described by the mathematical model:

$$\gamma_{3i} = a_i - c_i \cos(\zeta)\cos(\theta) \tag{4.4}$$

Error Bars: 95% CI over trials on three different days.

(a)

Error Bars: 95% CI over trials on three different days.
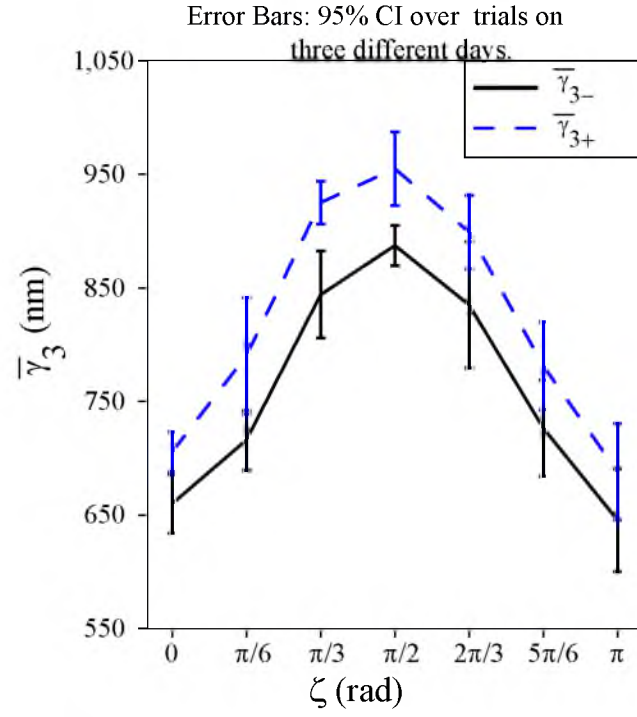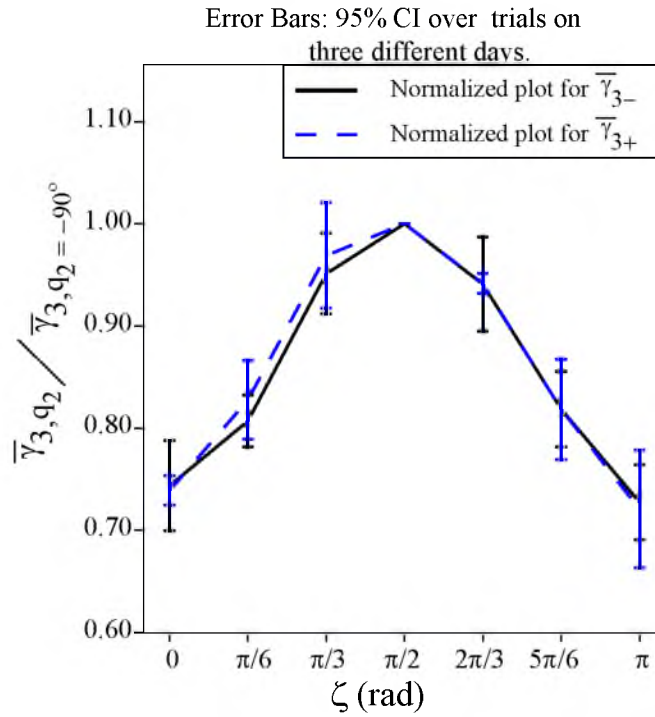
(b)

Figure 4.8. (a) Variation in step size, $\overline{\gamma}_{3i}$, with change in q_2 with no gravitational force acting along the axis of the prismatic joint. (b) γ_{3i} from (a) normalized by γ_{i3} at $q_2 = \frac{-\pi}{2}$.
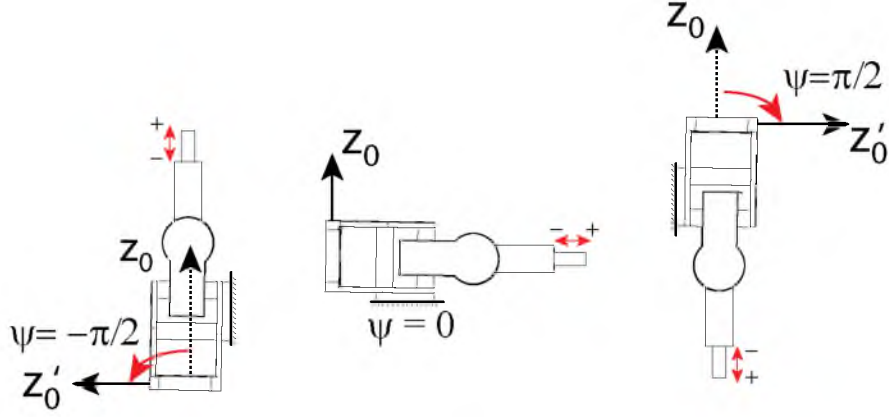
Figure 4.9. Configuration of the manipulator at $\psi = \frac{\pi}{2}$, 0, and $-\frac{\pi}{2}$, with $q_2 = -\frac{\pi}{2}$ and $\theta = 0$. ψ is varied from $-\frac{\pi}{2}$ to $\frac{\pi}{2}$ in steps of $\frac{\pi}{6}$.
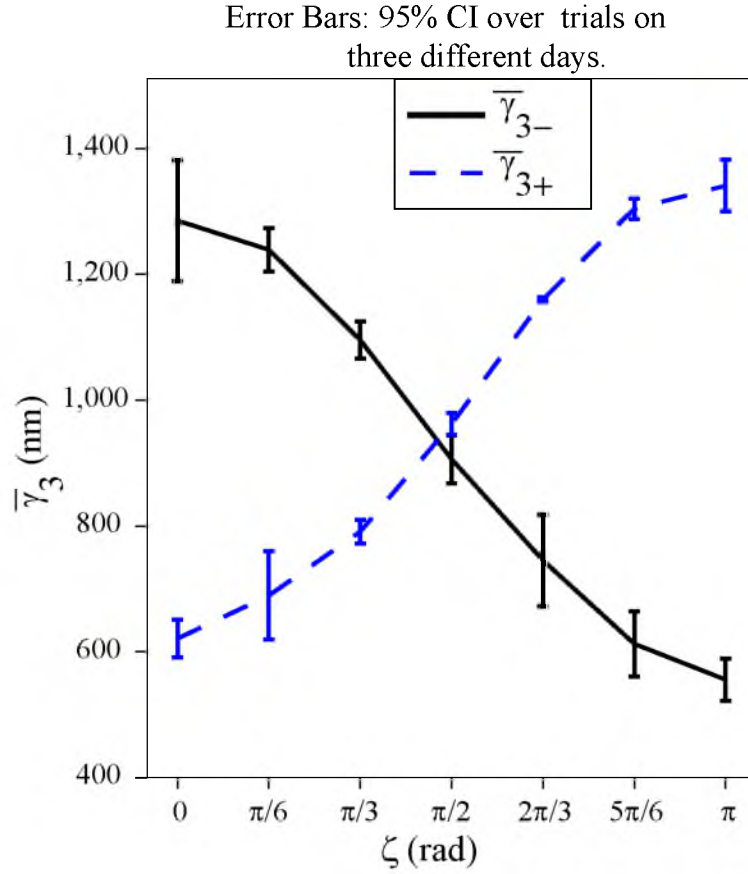
Figure 4.10. Plot showing the change in step size $\overline{\gamma}_{3i}$ with change in gravitational force achieved by changing ψ, with $q_2 = -\frac{\pi}{2}$ and $\theta = 0$.

where a_i and c_i are free parameters to be determined through calibration. The parameter a_i represents the basic step size of the joint when no gravitational load or recoil inefficiency is acting on the joint, and the parameter $c_i \cos(\zeta) \cos(\theta)$ represents a function of the component of the gravitational load due to the weight of the joint acting along the axis of the joint. As per our equation for the dynamics of the Kleindiek MM3A, Eq. A.114, the force acting on the prismatic joint is a function the cosine of the joint angle q_2 when the base frame is fixed. Comparing this with Eq. 4.4, we conclude that the γ_{3i} is also a function of the cosine of joint angle q_2, since $\zeta = \psi - q_2$.

In order to analyze the change in step size with change in joint variable q_3, an experiment was conducted wherein the prismatic joint was commanded a fixed number of steps, and the subsequent distance travelled (q_3) was measured. The manipulator was fixed at $q_2 = $ -$\frac{\pi}{2}$, $\theta = 0$, and $\psi = 0$. The measurements were collected by processing a microscopic image of the prismatic joint after every N number of steps. Fig. 4.11 shows the results of this experiment. Three readings each in inward and outward direction were taken on a single day separated by a fixed time. We can clearly see the the change in q_3 is approximately linear with the number of steps (N) commanded. From this we can safely conclude that the step size does not vary significantly throughout the range of motion of joint variable q_3.

4.7   Model for Static loads on Prismatic Joint

Fig. 4.12 shows the manipulator in three different configurations of q_2, with $\theta = 0$ and $\psi = 0$. It describes the sequence of the configuration of the manipulator at which γ_{3i} was recorded at $\theta = 0$. Similarly, γ_{3i} was recorded at other different values of θ.

As can be seen from the results obtained in Section 4.5, the step size taken by the prismatic joint is not constant when no gravitational force is acting on it. Rather, it is a function of q_2 as described by Eq. 4.3. The pure effect of gravity on the step size of the joint observed in Section 4.6 is modified by the position of the rotary joint q_2. This leads us to propose that the effect of gravity, represented by Eq. 4.4, and the effect of joint angle q_2, represented by Eq. 4.3, are coupled. A model, given by Eq. 4.5, takes into account both of these effects and is able to predict γ_{3i} at any configuration.

$$\gamma_{3i} \quad = \quad (1 - b_i |\cos(q_2)|)(a_i - c_i \cos(\zeta) \cos(\theta)) \tag{4.5}$$

where the terms have the same meanings as described before.

The predicted plots, showing the change in step size at $\theta = 0$ and $\theta = -\pi/3$, were obtained using values of the free parameters after calibration and were found to be accurate with $\pm 15\%$, details of which will be discussed in Chapter 6. The change in step size at

(a)

(b)
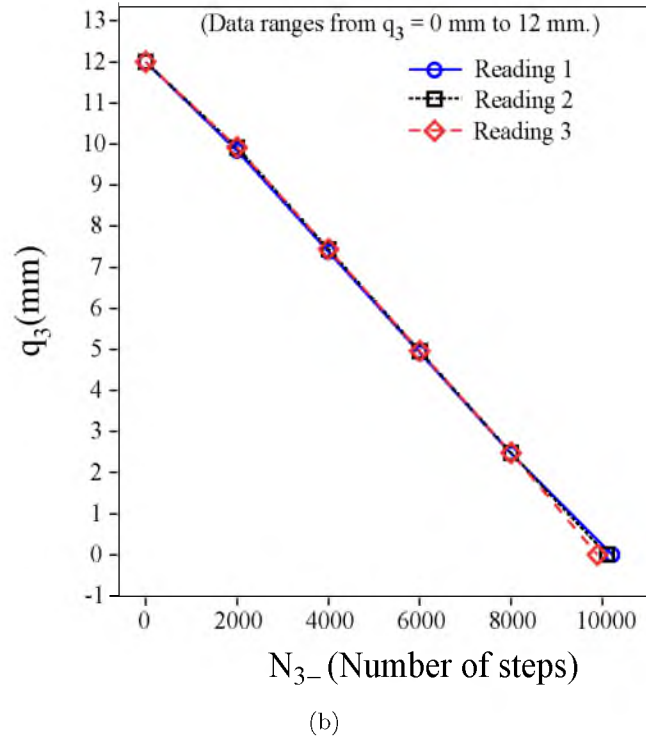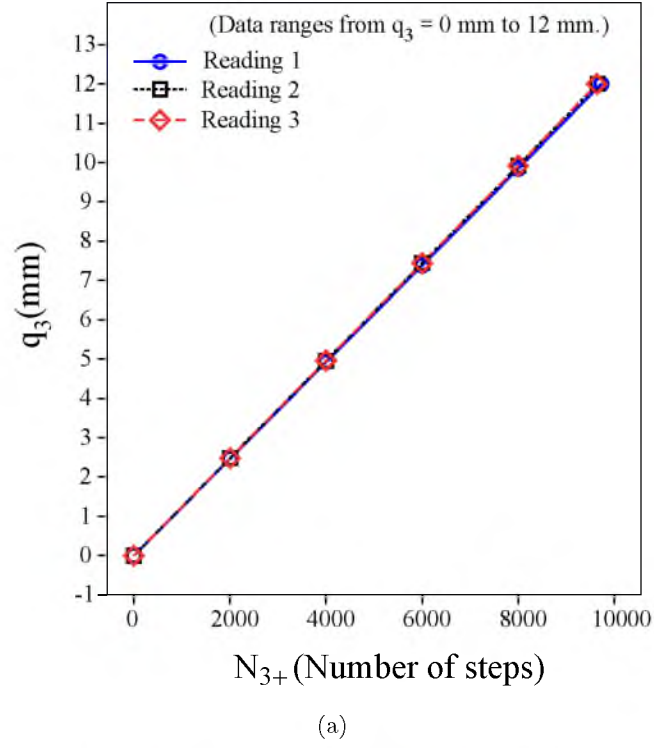
Figure 4.11. Experimental results showing the distance travelled by the prismatic joint as a function of the number of steps (N) commanded in the (a) outward direction, and (b) inward direction. The position is measured from a microscopic image of pixel size of 54.79 μm.
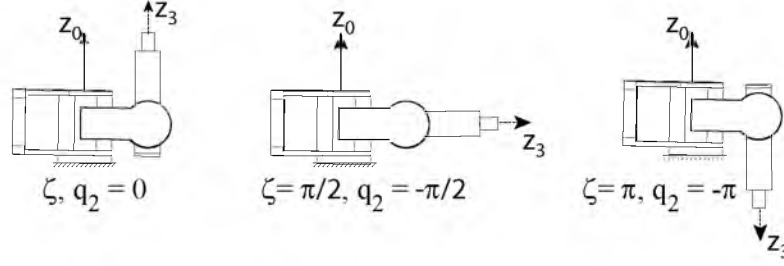
Figure 4.12. Configuration of the manipulator at $q_2 = 0$, $-\frac{\pi}{2}$ and $-\pi$, with ψ and θ fixed at 0. q_2 is varied from 0 to $-\pi$ in steps of $-\frac{\pi}{6}$.

$\theta = 0$ and $\theta = -\pi/3$ are shown by Figures 4.13(a) and 4.13(b), respectively. Based on the working principle of the piezoelectric stick-slip actuators as shown in Fig. 1.1, the step size in the desired motion should decrease with increase in the opposing gravitational load (as is seen in Fig. 4.10) as an increase of this load would make tracking the rapid movement of the piezoelectric element much easier and thus, mitigate the effectiveness of the "slip" phase. However, a closer look into the effect of q_2 as shown in 4.5 leads us to believe that this unusual effect is owing to the recoil nature associated with changing joint angle q_2, as discussed in Section 4.5.

(a)

(b)
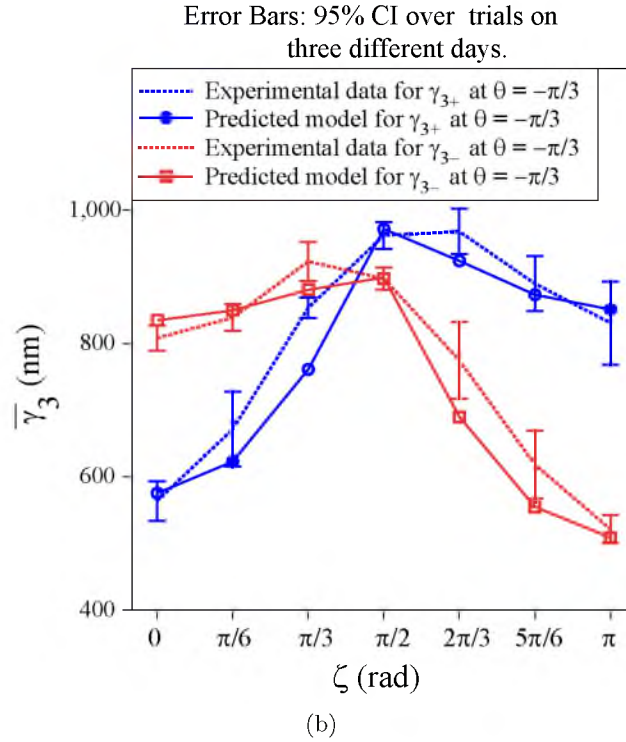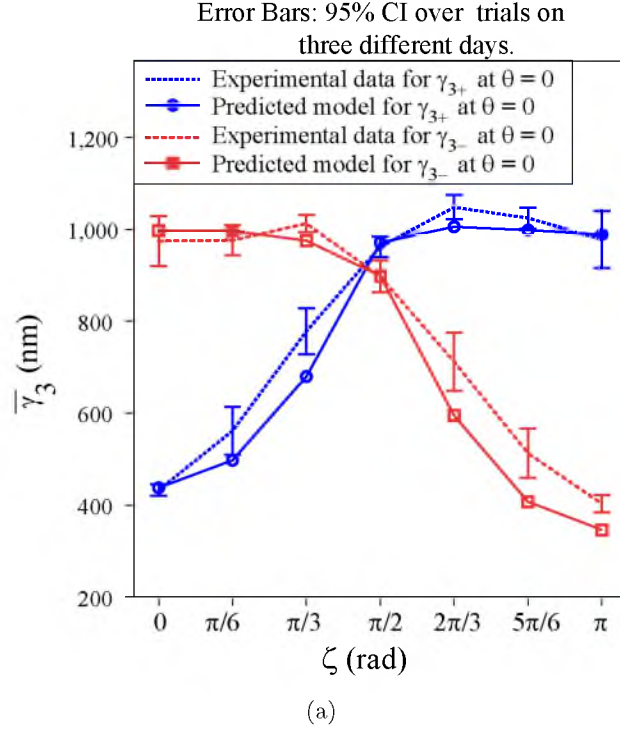
Figure 4.13. Effect of static loads on change in step size $\overline{\gamma}_{3i}$ at (a) $\theta = 0$ and $\psi = 0$, and (b) at $\theta = -\frac{\pi}{3}$ and $\psi = 0$. Predicted model equation computed using experimental data for a single day. Calibrated parameter values of $a_+ = 972$, $b_+ = 0.27$, and $c_+ = 375.55$, and $a_- = 899$, $b_- = 0.25$, and $c_- = $ -436 were found using the three calibration configurations described in the Chapter 6.

CHAPTER 5

MODEL OF THE ROTARY JOINT

The Kleindiek MM3A consists of two rotary joints, denoted by variables q_1 and q_2. The range of these rotary actuators is $240\,°$. The resolution for the rotary actuators, as specified by Kleindiek, is 10^{-7} radians and the range of the actuator utilizing the piezoelectric effect is 4×10^{-4} radians. Since joints 1 and 2 are both rotary joints having the same NanoMotor® as described in 2.1, both the joints are expected to have the same behavioral trend, the change only being in the inertial load on the respective joints. Thus, we are going to explore the behavior of joint 2 with respect to static and inertial loads, the results of which can be used to predict the behavior of joint 1 as well. Additionally, we expect the behavior of the rotary joints of other MM3A manipulators to be basically the same. In this chapter, we propose a model for the analytical prediction of the step size for joint 2 and substantiate our claim via experiments. We also present ANOVA statistical analysis giving the significance of unmodeled environmental factors that vary from day to day.

5.1   Experimental Procedure

The average step size $\overline{\gamma}_{2i}$ for rotary joint 2 is calculated using:

$$\overline{\gamma}_{2i} = \frac{4\pi}{3N_{2i}} \times 1000000 \quad \mu rad \tag{5.1}$$

where R_2 is the range of motion (the full range of motion for joint 2 is $\frac{4\pi}{3}$), N_{2i} is the number of steps taken across the range of motion, measured using the audio limit switch described in Section 4.1, and $i \in \{+, -\}$ indicates the direction of joint motion.

Before the start of any experiment, the rotary joint is driven through its full range back and forth twice. This is done in an attempt to mitigate any transients in the data due to heating of the piezoelectric actuators; this effect has been explained in [51].

5.2   Effect of Unmodeled Environmental Factors

Environmental conditions (e.g., temperature, humidity) are uncontrolled in our experiments, so there is no accurate model incorporating these factors. To minimize these

unmodeled effects on the open-loop control of the Kleindiek MM3A, we propose to calibrate the joints before each session of use. This assumes that there is a significant change from day to day that warrants such recalibration, proof of which could be seen in Fig. 5.1(a). To substantiate this claim, the step size for rotary joint 2 in the positive (γ_{2+}) and negative (γ_{2-}) direction were taken on two different days, which would incorporate the change in environmental conditions.

Fig. 5.1(a) shows the change in the step size of the rotary joint over two different days. Three values of γ_{2+} and γ_{2-} are recorded on each day, with $q_3 = 0\,\mathrm{mm}$, $\theta = -\pi/2$, and $\psi = 0$. An ANOVA test on the data shows that the difference in step size on different days is statistically significant ($p < 0.05$) for both positive ($p = 0.033$) and negative ($p = 0.016$) directions. The ANOVA test also shows a significant difference ($p = 0.0000004$) in the step size between the positive and negative directions within a given day. Thus, calibration on the rotary joints is recommended each time the manipulator is to be used, and different calibration parameters should be found for each direction of motion.

(a)

(b)
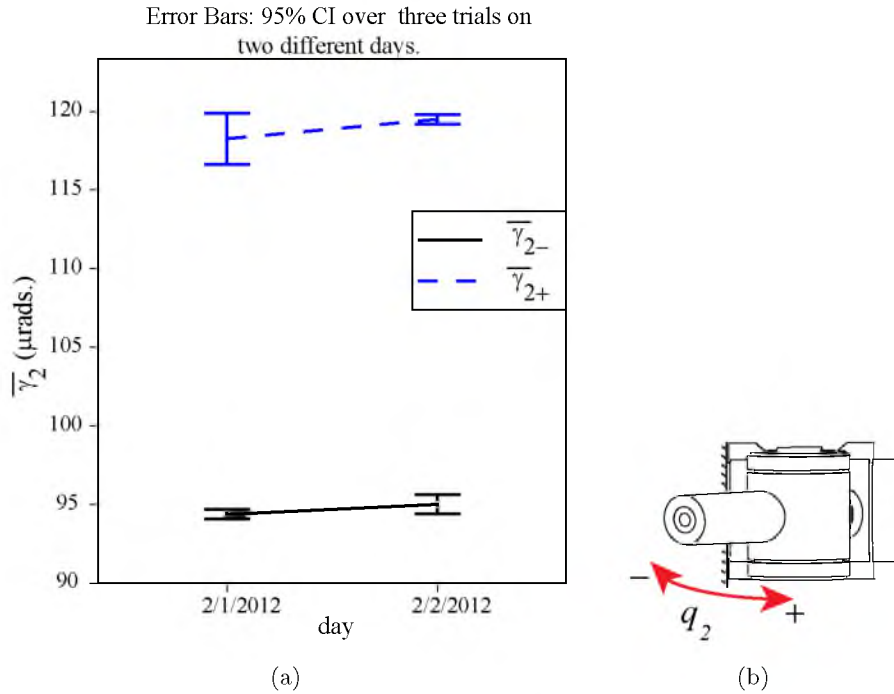
Figure 5.1. Plot showing (a) the change in step size, $\overline{\gamma}_2$ over two different days, and (b) the configuration of the manipulator at q_3=0 mm, θ=-$\pi/2$, and ψ=0, at which this experiment was conducted.

5.3 Effect of Static Loads

Fig. 5.2 shows two experiments that were performed to study the effect of gravitational loads on the rotary joint (in an effort to study static loading in general). In experiment 1, θ is kept at $-\pi/2$ such that there is no load due to gravity on the joint. In experiment 2, θ is kept at zero such that there is load due to gravity on the joint; here the gravitational load on joint 2 is a function of its own position q_2 (Fig. 5.3). This makes the study of gravitational loads on the rotary joints more challenging than that on the prismatic joints. To study the step size as a function of q_2, a fixture (Fig. 5.4) was developed to measure the average step size in intervals of $\pi/6$ in the range of $q_2 \in [0 \ -\pi]$. Starting with $q_2 = 0$, the number of steps required to move to q_2=-$\pi/6$ is measured using the fixture and the audio limit switch, and $\overline{\gamma}_{2-}$ is calculated for that interval. Similarly, the average step size is measured for subsequent intervals until $q_2 = -\pi$. These readings are taken for both $\theta = 0$ and $\theta = -\pi/2$, and for both negative ($\overline{\gamma}_{2-}$) and positive ($\overline{\gamma}_{2+}$) directions of motion, with two different values of q_3 (0 mm and 12 mm), as shown in Fig. 5.2. For both experiments, the step size values, taken at intervals of $\pi/6$, are plotted at the average value for q_2 in each interval (e.g., $\overline{\gamma}_{2-}$ measured for the interval $[0 \ -\pi/6]$ is plotted at $q_2 = -\pi/12$).

Fig. 5.5 shows the results of experiment 1, in which the variation of step size for $q_3 = 0$ mm at $\theta = -\pi/2$, from which it is safe to conclude that the step size of the rotary joint is relatively constant when no load due to gravity is acting on the joint; since the variation in step size in this configuration is found to be less than ±1–2%, with no discernible trend in the data. The normalization was performed by dividing the average step size values (at $\theta = -\pi/2$) obtained at each of the six fixed intervals by the total average of all these values. It can also be concluded that the step size γ_2 is not a function of q_2 in the absence of any loading, in either the positive or negative direction.

The model for static loading on the rotary joint is derived based on the physics that, if $\theta = 0$, the torque on joint 2 is related to gravitational loads as:

$$\tau_2 \propto g \sin(q_2) \tag{5.2}$$

where g is the acceleration due to gravity; the constant of proportionality is related to the mass and lengths of the distal links, which are unknown to us. The empirical model to predict the step size for the rotary joint is formulated as:

$$\gamma_{2i} = \gamma_{2i,\theta=-\pi/2} + d_i \sin(\zeta) \tag{5.3}$$

where $\gamma_{2i,\theta=-\pi/2}$ denotes the direction-dependent step size of the rotary joint when there is no effect of gravity on the link (i.e., at $\theta = -\pi/2$), d_i is a free parameter that denotes
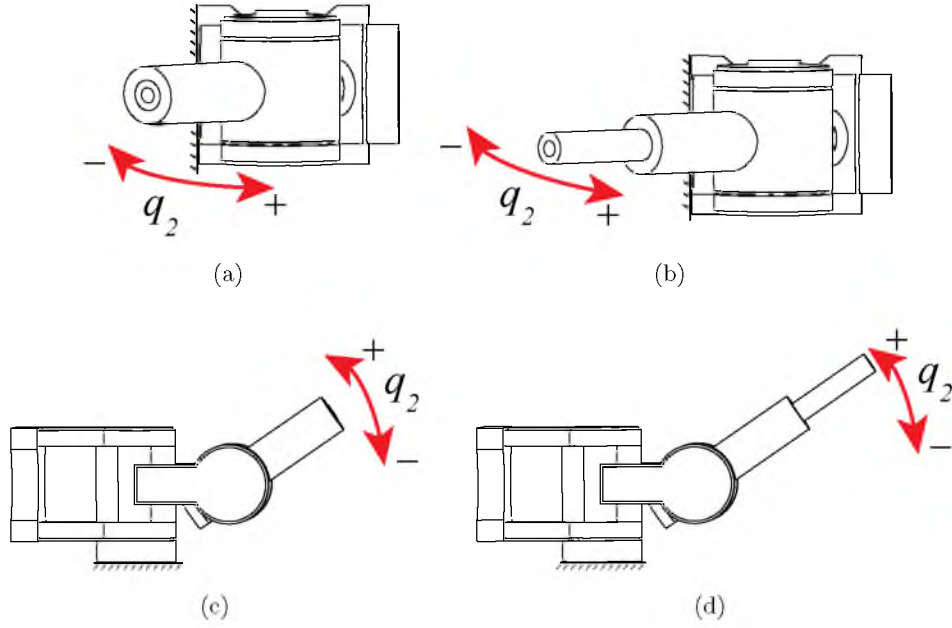
Figure 5.2. Configurations for experiments 1 and 2. (a) $\theta = -\pi/2$, $\psi = 0$, and $q_3 = 0\,\text{mm}$ (experiment 1); (b) $\theta = -\pi/2$, $\psi = 0$, and $q_3 = 12\,\text{mm}$ (experiment 1); (c) $\theta = 0$, $\psi = 0$, and $q_3 = 0\,\text{mm}$ (experiment 2); and (d) $\theta = 0$, $\psi = 0$ and $q_3 = 12\,\text{mm}$ (experiment 2).
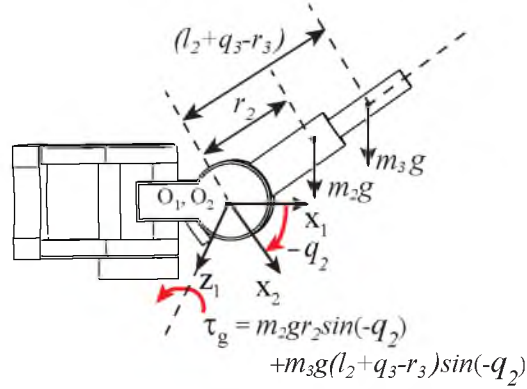
Figure 5.3. Loading due to gravity acting on joint 2 during experiment 2 ($\theta = 0$). This loading appears as an equivalent static torque load at the joint.

the maximum increase in step size over the basic step size $\gamma_{2i,\theta=-\pi/2}$, and $\zeta = \psi - q_2$ as described in Section 4.1. We assume that the step size at $\theta = -\pi/2$ and $\theta = \pi/2$ would be equal to the step size at $q_2 = 0$ and $q_2 = -\pi$ when $\psi = \theta = 0$, since there is no torque due to gravity on the joint in any of these cases. We expect d_i to vary linearly with q_3 since it encapsulates the gravitational load due to the center of mass of link 3; thus, two values for each d_i must be known to enable linear interpolation based on q_3.

Figure 5.4. Figure showing the stopper mechanism set up for the rotary joint.

The results of experiment 2 are shown in Fig. 5.6, which shows the effect of static loads on the step size of joint 2 when $\theta = 0$. The results show the mean and confidence intervals for experiments on three separate days. As we have already seen, the variance between days is quite large, so daily calibration is desirable (a predicted model is also shown, obtained from the calibration method discussed in the next chapter, but based on the calibration data from only one of the three days, hence its offset from the mean). As can be seen from the figure, the nature of step size in the positive direction is an inverted form of its nature in the negative direction. This is attributed to the fact that the load due to gravity acts against the direction of motion of the joint in the positive direction, and with it in the negative direction. Hence, the step size obtained in the positive direction, γ_{2+}, will be less than that obtained at $\theta = -\pi/2$ where no gravitation load is acting on the joint. The opposite holds true for the step size in negative direction, γ_{2-}. In other words, downward steps are bigger than horizontal steps, which in turn are bigger than upward steps, as we would expect.

If the manipulator were to be tilted by an angle $\theta \neq 0$, then the torque due to gravity on joint 2 would become proportional to the cosine of the gravitational component shown in equation 5.2, such that the model of equation 5.3 should be modified as:

$$\gamma_{2i} = \gamma_{2i,\theta=-\pi/2} + d_i \sin(\zeta) \cos(\theta) \tag{5.4}$$

5.4 Effect of Inertial Loads

Inertia plays a significant role in determining the step size of the joints of the Kleindiek MM3A. In Chapters 4, we only studied the effect of static loads on the prismatic joint, with the understanding that calibration would be used to account for the change in step size of the joint with any additional load attached to the end-effector. Now, we will briefly discuss the effect of increase in inertial load on the rotary joint of the MM3A, as the inertia loads
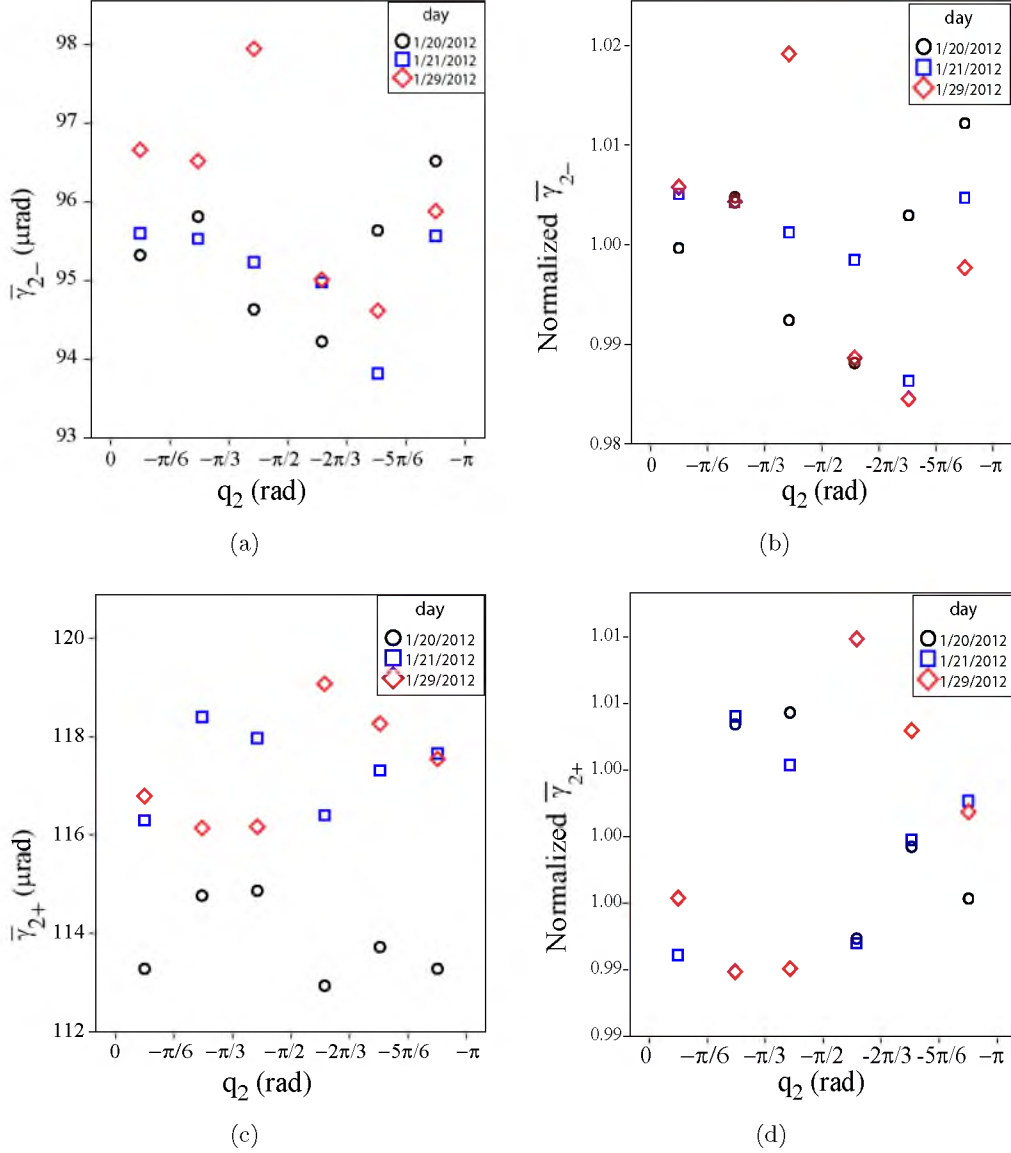
Figure 5.5. Experiment 1, corresponding to Fig. 5.2 and 5.2(a), with $\theta = -\pi/2$ and $\psi = 0$. (a) $\overline{\gamma}_{2-}$, (b) data in (a) normalized the average of the six values across the full range, (c) $\overline{\gamma}_{2+}$, and (d) data in (c) normalized the average of the six values across the full range.

will change with the configuration of the manipulator, so we cannot safely assume they will be constant during operation of the manipulator between calibrations.

In rotary joint 2, the inertial load acting on joint changes with q_3. Thus, the average step size for joint 2, $\overline{\gamma}_2$ was recorded at different values of $q_3 = 0$, 4, 8, and $12\,\text{mm}$ to study the effect of inertial load on the step size. Fig. 5.7 shows the change in step size with the change in q_3. The step size data was recorded at $\theta = -\pi/2$ so as to eliminate any effect of gravity, such that the variation in $\overline{\gamma}_2$ observed is purely due to a change in inertial load. The inertia
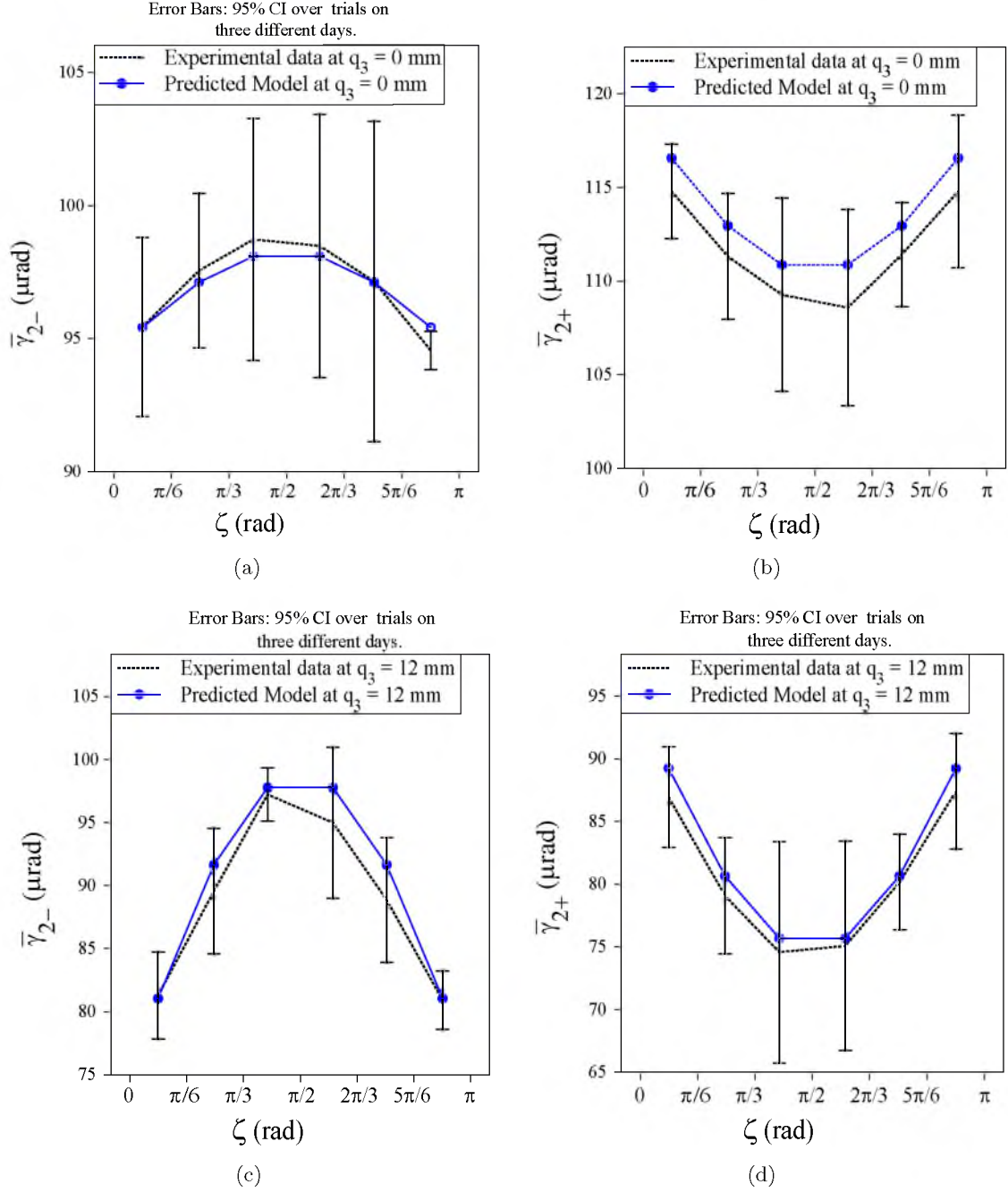
Figure 5.6. Experiment 2. Step size $\overline{\gamma}_{2i}$ as a function of ζ at (a) $q_3 = 0$ mm, $\psi = 0$, and $\theta = 0$ in the negative direction, with calibration parameter $d_- = 3.83\,\mu$rad, (b) $q_3 = 0$ mm, $\psi = 0$, and $\theta = 0$ in the positive direction, with calibration parameter $d_+ = -8.15\,\mu$rad, (c) $q_3 = 12$ mm, $\psi = 0$, and $\theta = 0$ in the negative direction, with calibration parameter $d_- = 23.94\,\mu$rad, and (d) $q_3 = 12$ mm, $\psi = 0$, and $\theta = 0$ in the positive direction with calibration parameter $d_+ = -19.40\,\mu$rad.
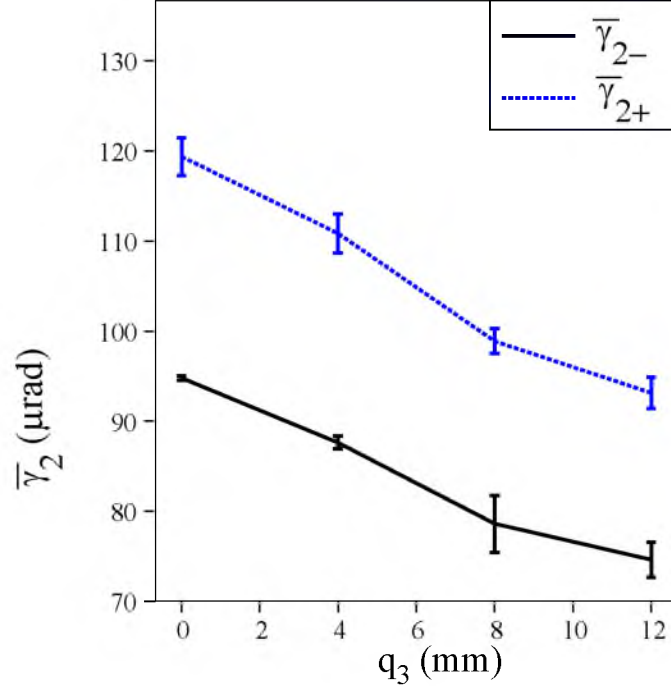
Figure 5.7. Effect of inertial loads on the step size of the rotary joint. The inertial load increases from $q_3 = 0\,\text{mm}$ to $12\,\text{mm}$, as the moment arm of the center of mass of link 3 increases with q_3. The configuration of the manipulator is kept at $\theta = -\pi/2$ and $\psi = 0$, such that gravity does not load the joint in question.

of a body with respect to a joint is directly proportional to the square of the perpendicular distance of the center of mass of the body to the joint axis due to the parallel-axis theorem, so the inertial load acting on the rotary joint due to q_3 should affect $\overline{\gamma}_2$ quadratically. Also, based on the stick-slip principle, we might expect that an increase in inertial load would reduce the return travel of the slider in the slip phase, resulting in an increase in the step size. However, we observe that the step size of the rotary joint decreases almost linearly with an increase in q_3 (or increase in inertial load). This contradicts our hypothesis that the step size of a joint generally increases with increase in inertial load. It might be possible that the displacement of the piezoelectric actuator in the stick phase is reduced due to the increase in inertial load, resulting in an overall reduction in step size with an increase in inertial load. Further research is required to explain this observed behavior. In this thesis, we will assume that the step size of joint 2 due to inertial effects of link 3 varies linearly with q_3. This means we must consider that $\gamma_{2i,\theta=-\pi/2}$ is a function of q_3; this will be considered in the following chapter.

CHAPTER 6

CALIBRATION TECHNIQUE

In this chapter, we discuss a calibration routine that can be used to identify the parameters of the models for the prismatic and rotary joint that were developed in chapters 4 and 5. The function obtained for the step size of joint j is of the form $\gamma_{ji} = \Gamma_{ji}(g, \alpha_i)$, where α_i is a set of actuator-specific parameters that will be obtained via calibration by using measurements of $\overline{\gamma}_{ji}$ at selected configurations for each joint. We will conclude this chapter by giving an effective calibration routine for the prismatic joint and the rotary joint 2 of the Keindiek MM3A. The step size model obtained by such a calibration technique can be used with previously developed methods described in [34] to perform open-loop control of the end-effector.

6.1   Prismatic Joint

The step size model for the prismatic joint as described in Eq. 4.5 is given by:

$$\gamma_{3i} \quad = \quad (1 - b_i|\cos(q_2)|)(a_i - c_i\cos(\zeta)\cos(\theta)) \tag{6.1}$$

where the subscript i denotes $+$ or $-$ direction.

This model has six unknown parameters that can be calibrated for by taking six measurements of $\overline{\gamma}_3$ as shown in Fig. 6.1. For simplicity, the average step size at a known configuration of q_2, θ, and ψ is denoted by $\overline{\gamma}_{3i(q_2,\theta,\psi)}$. The following procedure is used to identify the six free parameters $\alpha_3 = \{a_+, a_-, b_+, b_-, c_+, c_-\}$ of the prismatic joint:

(1) The prismatic joint is driven across its full range twice at θ and ψ equal to 0, so as to minimize the thermal effect as is discussed before.

(2) The average step size $\overline{\gamma}_{3+(-\pi/2,0,0)}$ and $\overline{\gamma}_{3-(-\pi/2,0,0)}$ for outward and inward directions, respectively, are measured at $(q_2, \theta, \psi) = (\frac{-\pi}{2}, 0, 0)$. By substituting these values in Eq. 6.1, we find parameter a_i of the model by the following relation

$$a_i \quad = \quad \overline{\gamma}_{3i(-\pi/2,0,0)} \tag{6.2}$$

Figure 6.1. Calibrating configurations (in sequence) for identifying the six unknown parameters of the model of the prismatic joint (joint 3). (a) a_i is calculated by measuring $\overline{\gamma}_{3i}$ at $(q_2, \theta, \psi) = (-\frac{\pi}{2}, 0, 0)$, (b) b_i is calculated using a_i calculated in the previous step and $\overline{\gamma}_{3i}$ at $(q_2, \theta, \psi) = (0, -\frac{\pi}{2}, 0)$, and (c) c_i is calculated using the values of a_i and b_i above, and $\overline{\gamma}_{3i}$ at $(q_2, \theta, \psi) = (0, 0, 0)$.

(3) Next, the prismatic joint is driven outward and then inward, from 0 to 12 mm and back, at a configuration of $q_2 = 0$, $\theta = -\pi/2$, and $\psi = 0$. The average step size $\overline{\gamma}_{3+(0,-\pi/2,0)}$ and $\overline{\gamma}_{3-(0,-\pi/2,0)}$ for outward and inward directions, respectively, are measured at $(q_2, \theta, \psi) = (0, \frac{-\pi}{2}, 0)$. By substituting these values in Eq. 6.1 and using the calculated value of a_i, we find parameter b_i using the following relation:

$$b_i = 1 - \frac{\overline{\gamma}_{3i(0,-\pi/2,0)}}{a_i} \tag{6.3}$$

(4) Finally, the average step size $\overline{\gamma}_{3+(0,0,0)}$ and $\overline{\gamma}_{3-(0,0,0)}$ for outward and inward directions, respectively, are measured at $(q_2, \theta, \psi) = (0, 0, 0)$, and by substituting these values in Eq. 6.1 along with a_i and b_i, we find parameter c_i using the following relation:

$$c_i = a_i - \frac{\overline{\gamma}_{3i(0,0,0)}}{1 - b_i} \tag{6.4}$$

Fig. 6.2 shows the predicted model and actual experimental data for a single day at $\theta = 0$ and $-\pi/3$. The value of $\theta = -\pi/3$ is not included as one of the calibration configurations, yet the model captures the step size of the joint as a function of the configuration. The accuracy of the predicted model was found to be within $\pm 20\%$ (within 100 nm).

6.2   Rotary Joint

The step size model for the rotary joint as described in Eq. 5.3 is given by:

$$\gamma_{2i} = \gamma_{2i,\theta=-\pi/2} + d_i \sin(\zeta) \tag{6.5}$$

Fig. 6.3 shows the calibration sequence for rotary joint 2, which would eventually give us values for the joint specific parameter, d and $\overline{\gamma}_{2,\theta=-\pi/2}$, for the rotary joint in the clockwise (-) and counterclockwise (+) direction respectively. For simplicity, the average step size at
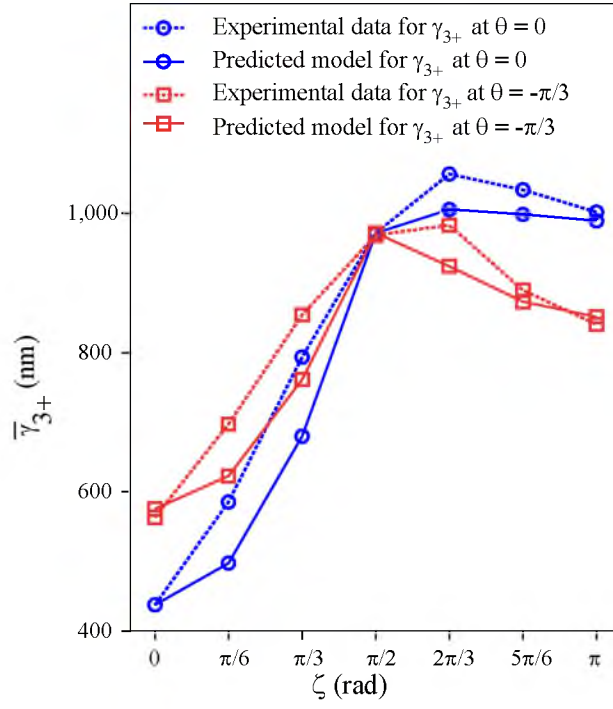
(a)
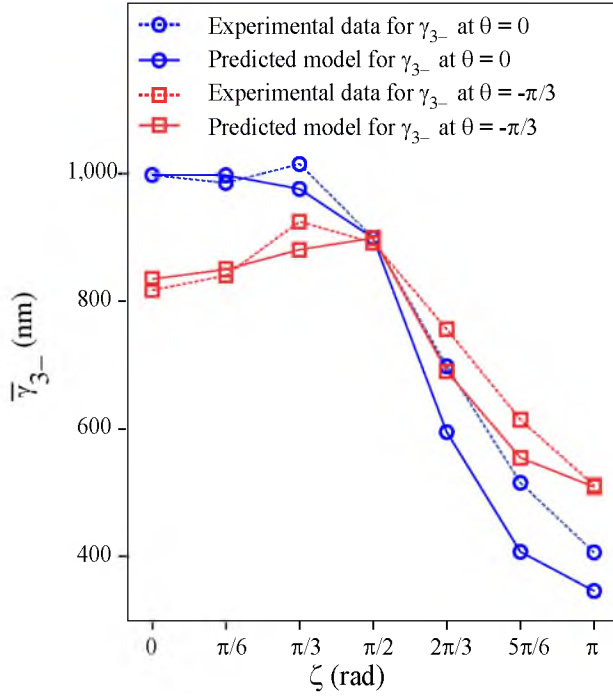
(b)

Figure 6.2. Predicted model at (a) $\theta = 0$ and $-\frac{\pi}{3}$ with $\psi = 0$ in the outward direction, and (b) $\theta = 0$ and $-\frac{\pi}{3}$ with $\psi = 0$ in the inward direction. The calibration parameter values are the same used in Section 4.7.
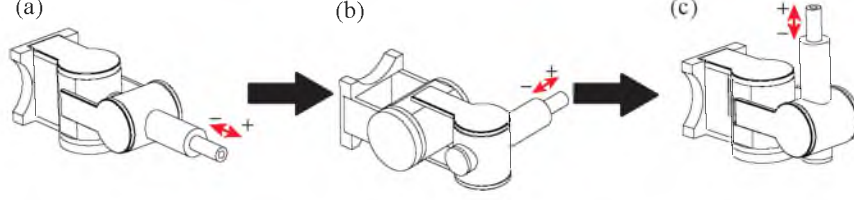
Figure 6.3. Calibrating configurations (in sequence) for identifying the six unknown parameters of the model of the rotary joint (joint 2). q_2 is driven across its full range from $\frac{\pi}{6}$ to $-\frac{7\pi}{6}$ in the negative and positive directions at (a) $q_3 = 0\,\text{mm}$, $\theta = 0$, and $\psi = 0$; (b) $q_3 = 12\,\text{mm}$, $\theta = 0$, and $\psi = 0$; (c) $q_3 = 0\,\text{mm}$, $\theta = \frac{-\pi}{2}$, and $\psi = 0$; and (d) $q_3 = 12\,\text{mm}$, $\theta = \frac{-\pi}{2}$, and $\psi = 0$.

a known configuration of q_3, θ and ψ is denoted by $\overline{\gamma}_{2(q_3,\theta,\psi)}$ unless otherwise mentioned. The following procedure is followed to obtain the free parameter:

(1) The rotary joint is driven across its full range twice at θ and ψ equal to 0, so as to minimize thermal effect as is discussed before.

(2) Joint 2 is driven across its range from $q_2 = \pi/6$ to $-7\pi/6$ in the negative direction and then in the positive direction at $q_3 = 0\,\text{mm}$ with $\theta = 0$ and $\psi = 0$. The step size data obtained is denoted as $\overline{\gamma}_{2-(0,0,0)}$ and $\overline{\gamma}_{2+(0,0,0)}$ for the negative and positive directions, respectively.

(3) Joint 2 then is driven across its range from $q_2 = \pi/6$ to $-7\pi/6$ in the negative direction and then in the positive direction at $q_3 = 12\,\text{mm}$ with $\theta = 0$ and $\psi = 0$. The step size data obtained is denoted as $\overline{\gamma}_{2-(12,0,0)}$ and $\overline{\gamma}_{2+(12,0,0)}$ for the negative and positive directions, respectively.

(4) Joint 2 is then driven across its range at $\theta = -\pi/2$ from $q_2 = \pi/6$ to $-7\pi/6$ in the negative and then in the positive direction at $q_3 = 12\,\text{mm}$ and $\psi = 0$. The step size data obtained are denoted as $\overline{\gamma}_{2-(12,-\pi/2,0)}$ and $\overline{\gamma}_{2+(12,-\pi/2,0)}$ for the negative and the positive directions, respectively.

(5) Joint 2 is then driven across its range at $\theta = -\pi/2$ from $q_2 = \pi/6$ to $-7\pi/6$ in the negative and then in the positive direction at $q_3 = 0\,\text{mm}$ and $\psi = 0$. The step size data obtained are denoted as $\overline{\gamma}_{2-(0,-\pi/2,0)}$ and $\overline{\gamma}_{2+(0,-\pi/2,0)}$ for the negative and the positive directions, respectively.

Since γ_2 is a function of q_2 at each instant, it not a trivial task to calculate the parameter d_i from Eq. 6.5 by using the average step size values ($\overline{\gamma}_{2i}$) that are available to us. The following algorithm is used to estimate d_i. In short, a simulation calculates the number of steps required to move across the full range of motion for a given value of d_i, and then the value of d_i is adjusted until the number of steps matches the experiment.

Algorithm for computing the free parameter d_i of the rotary joint

1: **Input** $\overline{\gamma}_{2i,\theta=-\pi/2}$, $\overline{\gamma}_{2i,\theta=0}$

2: Give an initial estimate for d_i

       Iterate the value of d_i for convergence.

3: **for** $i = 1$ to 5 **do**

4:     Initialize $\zeta = -\frac{\pi}{6}$

5:     Initialize $j = 1$

6:     **while** $\zeta_j \leq \frac{7\pi}{6}$ **do**

7:         $\gamma_{2j,\theta=0} = \overline{\gamma}_{2,\theta=-\pi/2} + d_i \sin(\zeta_j)$

8:         $j = j + 1$

9:         $\zeta_j = \gamma_{2(j-1),\theta=0} + \zeta_{j-1}$

10:    **end while**

11:    $\overline{\gamma}'_{2,\theta=0} = \frac{\sum(\gamma_{2,\theta=0})}{j}$

12:    $\zeta = \sin^{-1}\left(\frac{\overline{\gamma}'_{2,\theta=0} - \overline{\gamma}_{2,\theta=-\pi/2}}{d}\right)$

13:    $d = \frac{\overline{\gamma}_{2,\theta=0} - \overline{\gamma}_{2,\theta=-\pi/2}}{\sin(\zeta)}$

14:    $error = \overline{\gamma}_{2,\theta=0} - \overline{\gamma}'_{2,\theta=0}$

15: **end for**

16: **Output** d_i

After inputting the experimental values found for $\overline{\gamma}_{2,\theta=0}$ and $\overline{\gamma}_{2,\theta=-\pi/2}$ in our simulation, we initially estimate the free parameter d_i. The code in the while loop gives us the position and the step size of link 2 at each instant from $\zeta = \frac{\pi}{6}$ to $-\frac{7\pi}{6}$. Using this, we compute the average simulated value $\overline{\gamma}'_{2,\theta=0}$. This average value would correspond to a position of link 2 within the entire range of ζ taken. Thus, the corresponding ζ value at which this step size occurs is computed; subsequently, we compute d_i. The updated value of d_i is then sent back in the loop, and the same procedure is followed. Thus, we solve for d_i using multiple iterations until convergence. The error between the computed ($\overline{\gamma}'_{2,\theta=0}$) and actual experimental value ($\overline{\gamma}_{2,\theta=0}$) was found to be less than 10^{-11} radians after 5 iterations.

Fig. 6.4 shows the simulation results obtained for the rotary joint after iterating q_2 from $\frac{\pi}{6}$ to $-\frac{7\pi}{6}$ (i.e., the range of q_2). This confirms the behavior of the rotary joint 2. For computing d_i in the algorithm above, we took values of $\overline{\gamma}_{2,\theta=-\pi/2}$ ranging from $75\,\mu$rad to $115\,\mu$rad with $\overline{\gamma}_{2,\theta=0}$ varying such that the difference between the two average step size values never exceeds its limit as found in experiments ($\pm 9.2\,\mu$rad). It was found that the difference between these two average step size values show a quadratic relationship with the free parameter d_i as shown in Fig. 6.5.
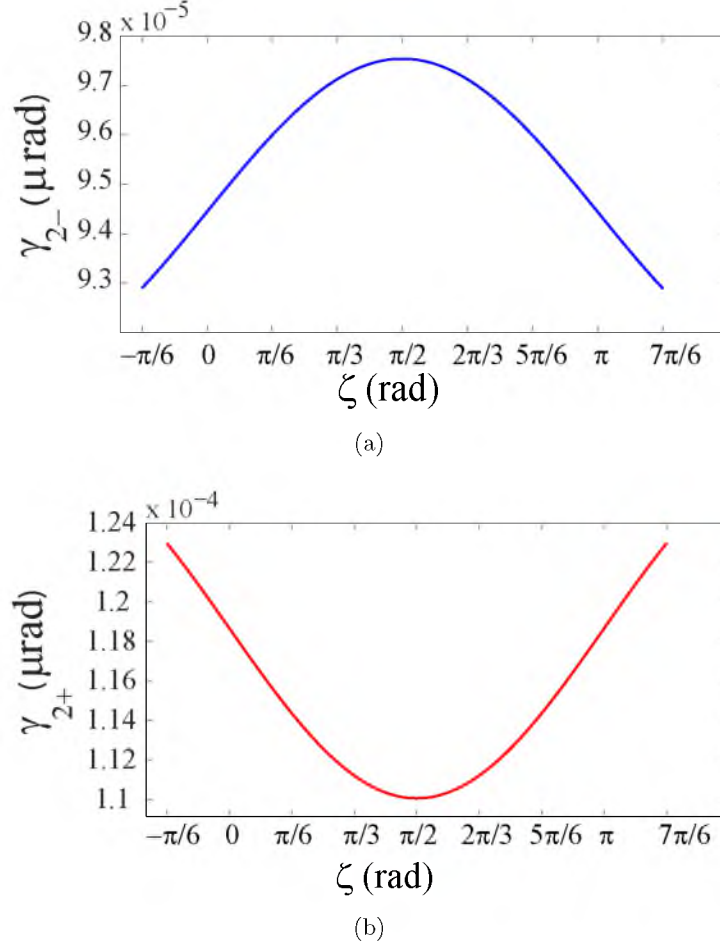
Figure 6.4. Simulated model of the step size of joint 2 in (a) the negative direction, and in (b) the positive direction. The values of $\overline{\gamma}_{2,\theta=0}$ and $\overline{\gamma}_{2,\theta=-\pi/2}$ are fixed.

As can be seen from Fig. 6.5, irrespective of the values of $\overline{\gamma}_{2,\theta=0}$ and $\overline{\gamma}_{2,\theta=-\pi/2}$, the free parameter value d_i remains almost the same (difference of $< 1\,\mu\,\mathrm{rad}$) for the same difference between the two step size values aforementioned. The parameter d_i was calculated using the value of $\overline{\gamma}_{2,\theta=0} - \overline{\gamma}_{2,\theta=-\pi/2}$ from $-9.2\,\mu\mathrm{rad}$ to $9.2\,\mu\mathrm{rad}$ as this was the range of $\overline{\gamma}_{2,\theta=0}$ - $\overline{\gamma}_{2,\theta=-\pi/2}$ observed in experiments. A relation for computing d_i was formulated by fitting the simulation results obtained to a quadratic function as shown in Fig. 6.5. The equation formulated using nonlinear least-squares regression is:

$$
\begin{aligned}
d_i &= 3.41(\overline{\gamma}_{2i,\theta=0} - \overline{\gamma}_{2i,\theta=-\pi/2})^2 + 0.025(\overline{\gamma}_{2i,\theta=0} - \overline{\gamma}_{2i,\theta=-\pi/2}) \\
&\quad + 6.42 \times 10^{-7}
\end{aligned}
\tag{6.6}
$$

Fig. 5.6 shows that there is a significant effect of the joint 3 variable q_3 on the step size of the rotary joint 2. Also, $\overline{\gamma}_{2i,\theta=-\pi/2}$ and d_i are functions of q_3. This is expected, as a
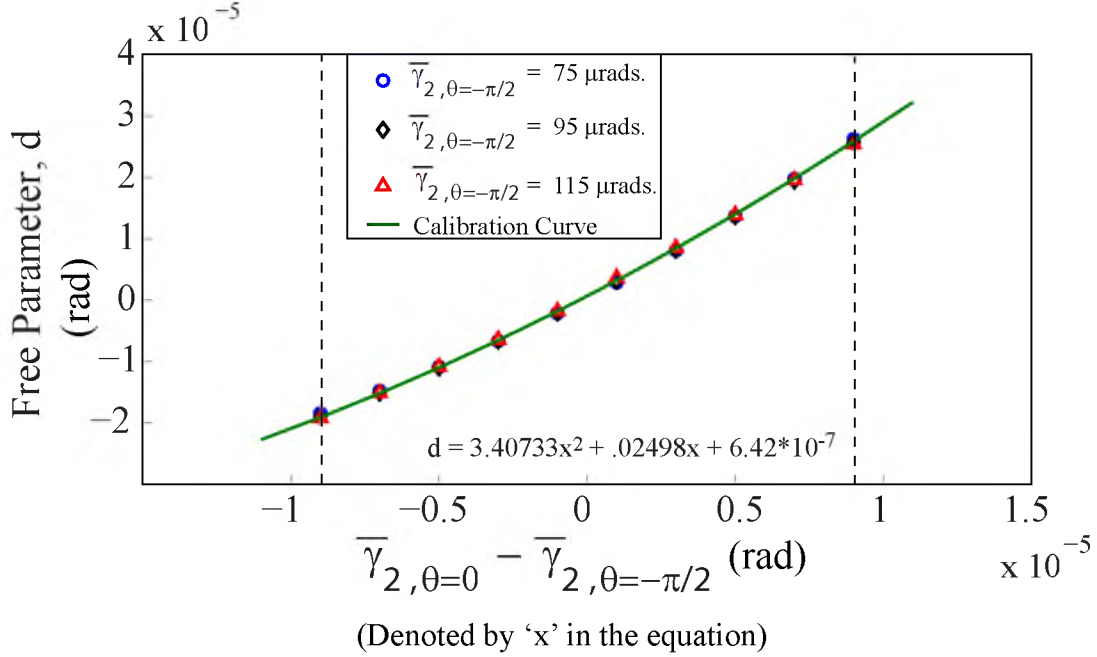
Figure 6.5. Variation of the free parameter with respect to change in difference between $\overline{\gamma}_{2,\theta=0}$ and $\overline{\gamma}_{2,\theta=-\pi/2}$ at different values of $\overline{\gamma}_{2,\theta=-\pi/2}$. The vertical dash lines represent the range of this difference as observed in experiments.

change in q_3 will lead to a change in inertial load on joint 2 and, as discussed in Chapter 5, a change in the step size of joint 2. We observed that $\overline{\gamma}_{2,\theta=-\pi/2}$ varies linearly with q_3 (Fig. 5.7) and hence, a linear-interpolation model for $\overline{\gamma}_{2,\theta=-\pi/2}$ and d_i would be a good approximation of the variation in the step size of joint 2 due to a change in q_3. Eq. 6.5 then becomes:

$$\gamma_{2i} = \gamma_{2i,\theta=-\pi/2}(q_3) + d_i(q_3)\sin(\zeta) \tag{6.7}$$

where i denotes $+$ or $-$ direction of the rotary joint, and

$$\gamma_{2i,\theta=-\pi/2}(q_3) = \gamma_{2i(0,-\pi/2,0)} + q_3\left(\frac{\gamma_{2i(12,-\pi/2,0)} - \gamma_{2i(0,-\pi/2,0)}}{12}\right) \tag{6.8}$$

$$d_i(q_3) = d_{i(0,-\pi/2,0)} + q_3\left(\frac{d_{i(12,-\pi/2,0)} - d_{i(0,-\pi/2,0)}}{12}\right) \tag{6.9}$$

Although the inertial load on joint 2 increases with q_3, our method for finding the free parameter d_i (Eq. 6.6) remains the same, as the change in step size due to an increase in inertial load due to q_3 is reflected as a change in $\overline{\gamma}_{2,\theta=-\pi/2}$ and $\overline{\gamma}_{2,\theta=0}$. So, for finding the free parameter d_i, it does not matter what values of q_3 we use.

Fig. 6.6 shows the predicted model after computing d_i via calibration against experimental data collected on a single day. Taking into account the effect of angle θ on the load acting on the rotary joint, the equation for predicting the step size of joint 2 would become:

$$\gamma_{2i} \quad = \quad \gamma_{2i,\theta=-\pi/2}(q_3) + d_i(q_3)\sin(\zeta)\cos(\theta) \tag{6.10}$$

Data were then collected at $\theta = -\pi/4$ and $\psi = 0$ to verify this model in a different configuration, results of which are shown in Fig. 6.7. The predicted models obtained after calibration, as shown in Figures 6.6 and 6.7, is found to be accurate to within $1\,\mu$rad or $\pm 2\%$.

Because joint 1 is another rotary joint with the same range as joint 2 and having the same properties except for the change in static load value, this model and calibration routine for joint 2 can be extended to joint 1. The only difference in the calibration routine would be that at $\theta = 0$ there is no effect of gravity on joint 1, while at $\theta = -\pi/2$ the gravity is perpendicular to the joint axis. So, in short the definition of the terms, $\overline{\gamma}_{2i,\theta=0}$ and $\overline{\gamma}_{2i,\theta=-\pi/2}$ would be interchanged.

To conclude, a total of 14 calibration routines (6 for the prismatic joint and 8 for the rotary joint) have been presented to predict the 14 free parameters of our empirically derived analytical model. The model can be used to predict the step size of the joints at a given manipulator configuration.

Figure 6.6. Predicted model (after calibration) at (a) $q_3 = 0\,\text{mm}$, $\theta = 0$, and $\psi = 0$ in the negative direction; (b) $q_3 = 0\,\text{mm}$, $\theta = 0$, and $\psi = 0$ in the positive direction; (c) $q_3 = 12\,\text{mm}$, $\theta = 0$, and $\psi = 0$ in the negative direction; (d) $q_3 = 12\,\text{mm}$, $\theta = 0$, and $\psi = 0$ in the positive direction.
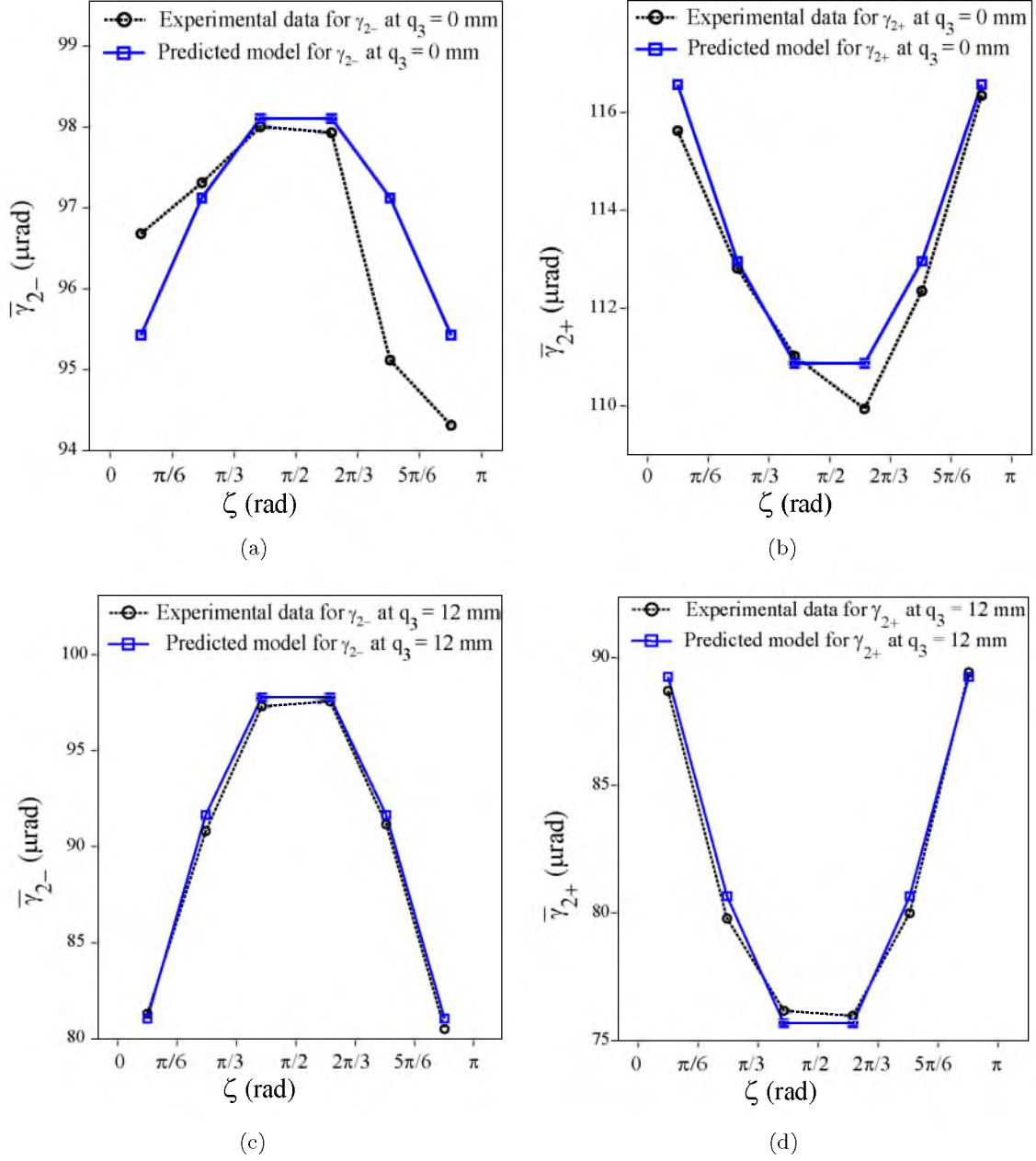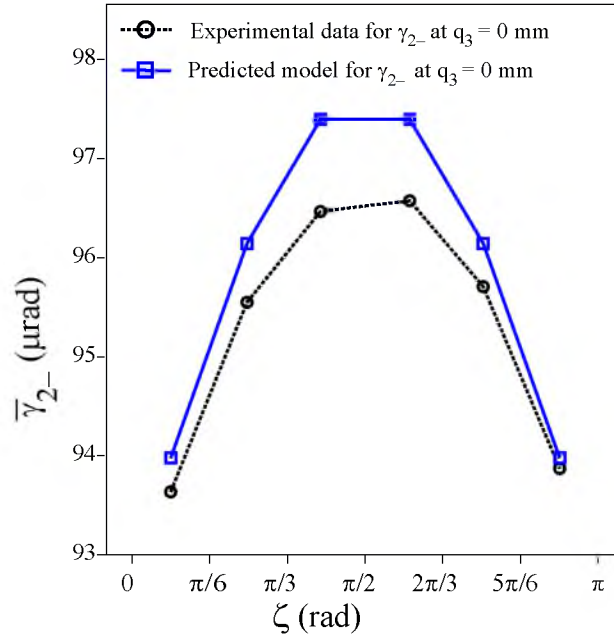
(a)
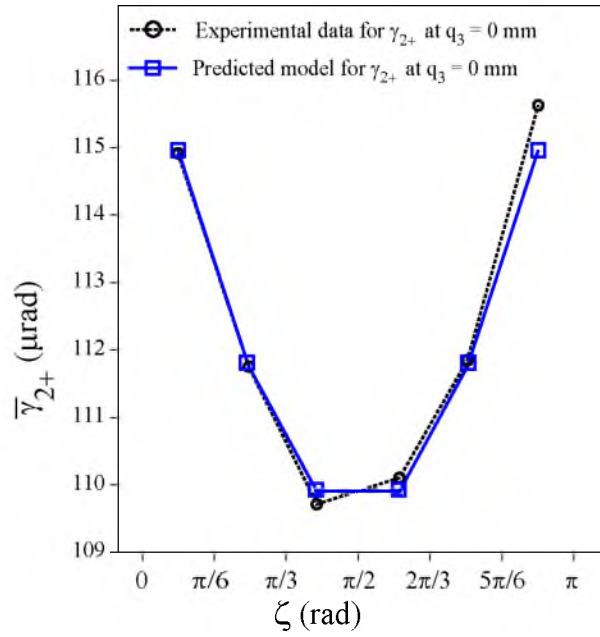
(b)

Figure 6.7. Predicted model (after calibration) at (a) $q_3 = 0\,\text{mm}$, $\theta = -\pi/4$, and $\psi = 0$ in the negative direction; (b) $q_3 = 0\,\text{mm}$, $\theta = -\pi/4$, and $\psi = 0$ in the positive direction.

CHAPTER 7

ACCURACY

Kleindiek does not give specifications describing the step size of each joint of the MM3A, so it is not possible for us to compare our method to some preexisting manufacturer specification. To compare our developed model with a simpler, less-sophisticated model, we analyzed our model in comparison with the constant step size obtained for both prismatic and rotary joint when there is no effect of gravity acting on the respective joints. This alternate method still requires the audio limit switch or some equivalent method to detect the range of travel (which has not been developed previously), but it does not require the more complicated model developed herein, and it is an alternative that one might expect to have reasonable predicting power.

From Fig. 7.1, we can conclude that the developed model of the prismatic joint is accurate to within 15% of the experimental results throughout the configuration of the manipulator, whereas the constant step size model predicts the step size well only at configurations when there is little influence of gravitational force. In the worst-case configuration, the simpler model has an error in step size that is approximately 10% of the actual experimental value. From Fig. 7.2, we can conclude that the developed model of the rotary joint is accurate to within 2% of the experimental model, whereas the constant step size model predicts the step size well only when the gravitational force acting on the rotary joint is minimal. In the worst-case configurations, the simpler model has an error that is approximately 1.3% of the actual experimental value.

From this analysis,we find that our developed model increases the overall accuracy with which the step size taken by the respective joints of the Kleindiek MM3A could be predicted, even when compared to a simpler model that would in itself be novel compared to the state of the art.
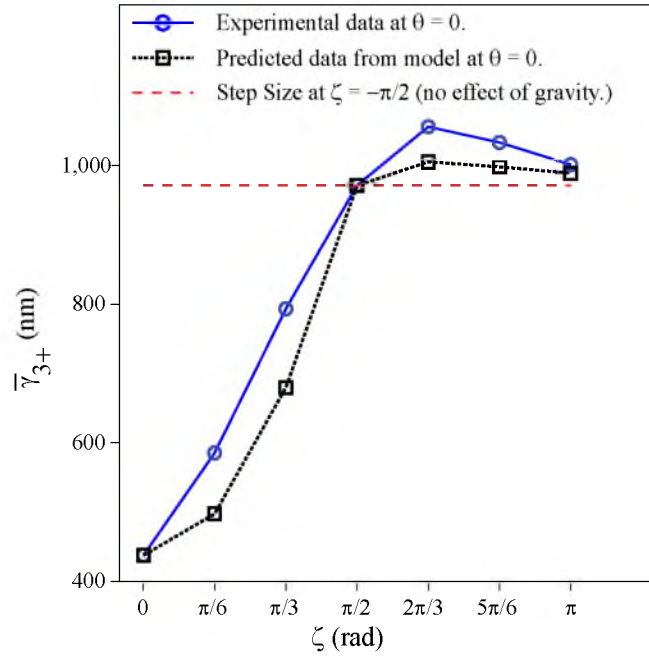
(a)
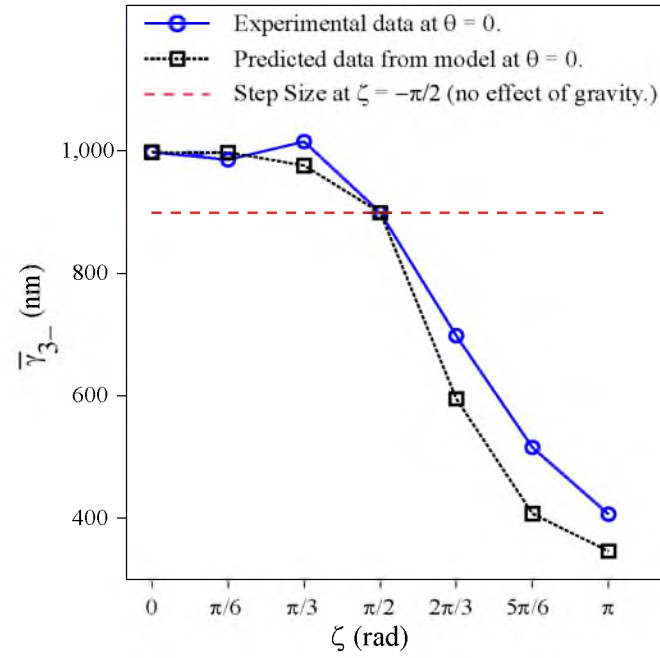
(b)

Figure 7.1. Comparison of our predicted model with the constant step size in the (a) outward direction, and (b) inward direction.
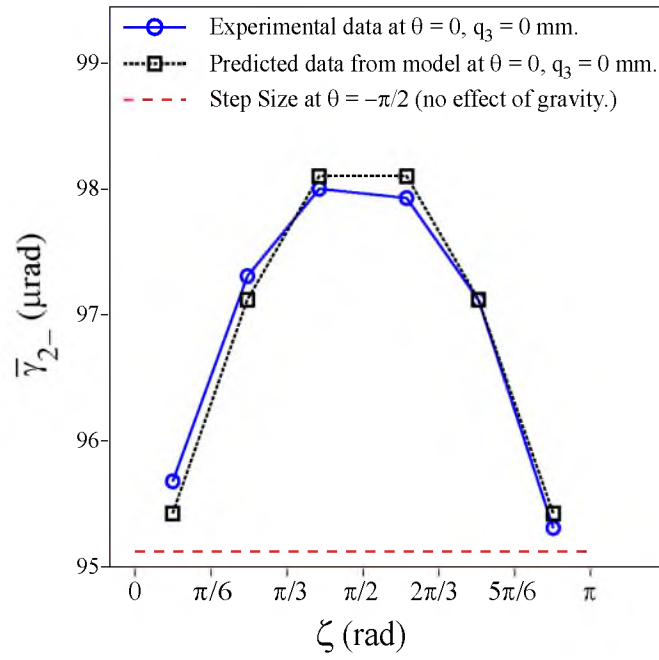
(a)
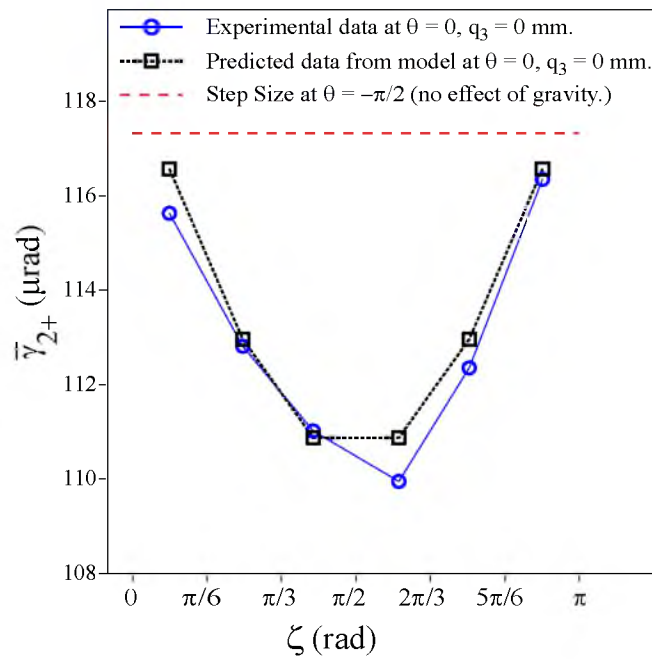
(b)

Figure 7.2. Comparison of our predicted model with the constant step size in the (a) − direction, and (b) + direction.

CHAPTER 8

CONCLUSION AND FUTURE WORK

The Kleindiek MM3A can be used in applications requiring high precision to the scale of a few nanometers, with larger steps on the order of $1\,\mu$m. For effective control of the manipulator, it is often utilized using a device such as an SEM. However, this machine is very expensive, and research groups end up paying \$50–\$100 per hour. With the open-loop control algorithm as developed in this thesis, one only requires a quick calibration routine involving taking step-size readings of the joints of the Kleindiek at specific configurations. This procedure described not only is cheaper, it is also easy to follow, and could result in significant savings in time. Several closed-loop schemes, and modeling techniques for effective manipulation of the piezoelectric stick-slip actuators, have been discussed in Chapters 1 and 2. In Chapter 3, we explained the dynamics of the Kleindiek MM3A by incorporating the fact that the joints of this manipulator are decoupled. We modeled static-loading effects on the prismatic joint (Chapter 4), and static- and inertial-loading effects on the rotary joint (Chapter 5) of the manipulator. In spite of the highly nonlinear nature of the piezoelectric actuators, it was found that there is a repeatable stochastic pattern that they follow that depends on the loads acting on the joint. This pattern can be modeled and used for effective open-loop control of the Kleindiek MM3A. In Chapter 6, we discussed the calibration techniques employed for predicting the step size of the joints of the manipulator in any configuration. The accuracy we achieved was within $\pm 15\%$ (100 nm) for prismatic joint and $\pm 2\%(2\,\mu$rads) for rotary joints.

In this work, we made the assumption that the joints are completely independent, in that a step in one joint has no effect in any of the other joints. This is a common assumption that appears accurate. We neglected any effect of dynamic coupling that may occur owing to its' backdrivable nature. Further research needs to be done to incorporate this phenomenon if it is important, or verify that it is not. The experiments in this thesis were performed using a single Kleindiek MM3A, but we expect the results to generalize to other MM3As and other similar devices that utilize piezoelectric stick-slip actuators. Having said this, the

effectiveness of this model has yet to be tested on other similar devices.

The next step in this research is to combine the open-loop model derived in this thesis with master-slave teleoperation algorithms. Such algorithms will enable a human user to command an end-effector velocity that is converted into necessary joint velocities, which in turn can be converted into a number of joint steps required. In this way, the micromanipulator can be controlled more like other robots, rather than by controlling individual joints as is currently done.

APPENDIX

DERIVATION OF THE KINEMATICS AND DYNAMICS OF THE KLEINDIEK MM3A MICROMANIPULATOR

In this appendix we derive the forward kinematics, inverse kinematics, manipulator Jacobian, and dynamic equations for the Kleindiek MM3A.

A.1   Forward Kinematics and Manipulator Jacobian

The Kleindiek MM3A is a serial link rotary-rotary-prismatic (RRP) manipulator. We model the MM3A as a 3-DOF robotic manipulator, as shown in Fig. 4.1, where the MM3A has been modeled using the Denavit-Hartenberg (D-H) convention. Table A.1 shows the D-H parameters for the manipulator concerned.

The system shown in Fig. 4.1 has four coordinate systems defined. Frame 0 represents the base frame, with joint 1 corresponding to rotation about $\vec{z_0}$. Frame 1 is attached to the first link and rotates about $\vec{z_0}$ by the angle q_1, with joint 2 corresponding to rotation about $\vec{z_1}$. Frame 2 is attached to the second link and rotates about $\vec{z_1}$ by the angle q_2, with joint 3 corresponding to translation along $\vec{z_2}$. The frame's origin O_2 is coincident with O_1, which is the origin of frame 1. A tool frame 3 is attached to the distal end of the third link and translates prismatically along $\vec{z_2}$ by q_3. It has an initial offset of l_2 from frame 2.

The homogeneous transformation matrix of frame 3 with respect to the base frame is:

Table A.1. D-H parameters for RRP manipulator.

i	a_i	d_i	α_i	θ_i
1	a_1	0	$\pi/2$	q_1
2	0	0	$-\pi/2$	q_2
3	0	$l_2 + q_3$	0	0

$$
{}^0T_3 \;=\; \begin{bmatrix} c_1c_2 & -s_1 & -c_1s_2 & -(l_2+q_3)c_1s_2 + a_1c_1 \\ s_1c_2 & c_1 & -s_1s_2 & -(l_2+q_3)s_1s_2 + a_1s_1 \\ s_2 & 0 & c_2 & (l_2+q_3)c_2 \\ 0 & 0 & 0 & 1 \end{bmatrix} \tag{A.1}
$$

where s_i and c_i represent the sine and cosine of the angle q_i, respectively. Consequently, we deduce the forward kinematics for the manipulator as:

$$
\begin{bmatrix} {}^0d_{03x} \\ {}^0d_{03y} \\ {}^0d_{03z} \end{bmatrix} = \begin{bmatrix} -(l_2+q_3)c_1s_2 + a_1c_1 \\ -(l_2+q_3)s_1s_2 + a_1s_1 \\ (l_2+q_3)c_2 \end{bmatrix} \tag{A.2}
$$

where ${}^0\vec{d}_{03}$ is the vector from O_0 to O_3, expressed with respect to frame 0.

The Manipulator Jacobian, $J(\vec{q})$ is of the form:

$$
\begin{bmatrix} {}^0\dot{d}_{03} \\ \omega_{03} \end{bmatrix} \;=\; J(\vec{q})\dot{\vec{q}} = \begin{bmatrix} (l_2+q_3)s_1s_2 - a_1s_1 & -(l_2+q_3)c_1c_2 & -c_1s_2 \\ -(l_2+q_3)c_1s_2 + a_1c_1 & -(l_2+q_3)s_1c_2 & -s_1s_2 \\ 0 & -(l_2+q_3)s_2 & c_2 \\ 0 & s_1 & 0 \\ 0 & -c_1 & 0 \\ 1 & 0 & 0 \end{bmatrix} \begin{bmatrix} \dot{q}_1 \\ \dot{q}_2 \\ \dot{q}_3 \end{bmatrix} \tag{A.3}
$$

A.2 Inverse Kinematics

For the inverse kinematics problem, we assume we are given ${}^0\vec{d}_{03}$, and our goal is to find the joint values $\vec{q}$. We will now derive the inverse kinematics equations to compute the joint values.

To solve for q_1, we look at the top view in Fig. A.1(a), finding:

$$
q_1 = atan2({}^0d_{03y}, {}^0d_{03x}) \tag{A.4}
$$

Next, to solve for q_2 we first compute

$$
{}^1d_{13} \equiv \begin{bmatrix} {}^1d_{13x} \\ {}^1d_{13y} \\ {}^1d_{13z} \end{bmatrix} = {}^0R_1^T({}^0d_{03} - {}^0d_{01}) \tag{A.5}
$$

Looking at the front view in Fig. A.1(b), we get

$$
q_2 = atan2({}^1d_{13y}, {}^1d_{13x}) \tag{A.6}
$$

Finally, to solve for q_3, we see that from Eq.(A.2),

$$
\begin{aligned}
({}^0d_{03x})^2 + ({}^0d_{03y})^2 + ({}^0d_{03z})^2 \;=\;& (-(q_3+l_2)c_1s_2 + a_1c_1)^2 + \\
& (-(q_3+l_2)s_1s_2 + a_1s_1)^2 + ((q_3+l_2)c_2)^2
\end{aligned} \tag{A.7}
$$

Solving, we get

$$q_3 = \frac{2a_1 s_2 \pm \sqrt{(2a_1 s_2)^2 - 4(a_1^2 - ((^0 d_{03x})^2 + (^0 d_{03y})^2 + (^0 d_{03z})^2))}}{2} - l_2$$

(A.8)

Thus, we have solved for the joint variables given the postion of frame 3 with respect to the base frame.

A.3 Dynamics

The Lagrangian formulation is used for computing the dynamics of the Kleindiek MM3A [54]. The *Lagrangian* of a mechanical system can be defined as a function of the generalized coordinates:

$$L = T - U$$

(A.9)

where T and U respectively denote the total *kinetic energy* and *potential energy* of the system. The Lagrange equations are expressed by:

$$\frac{d}{dt} \frac{\partial L}{\partial \dot{q}_i} - \frac{\partial L}{\partial q_i} = \tau_i \qquad i = 1,2,3$$
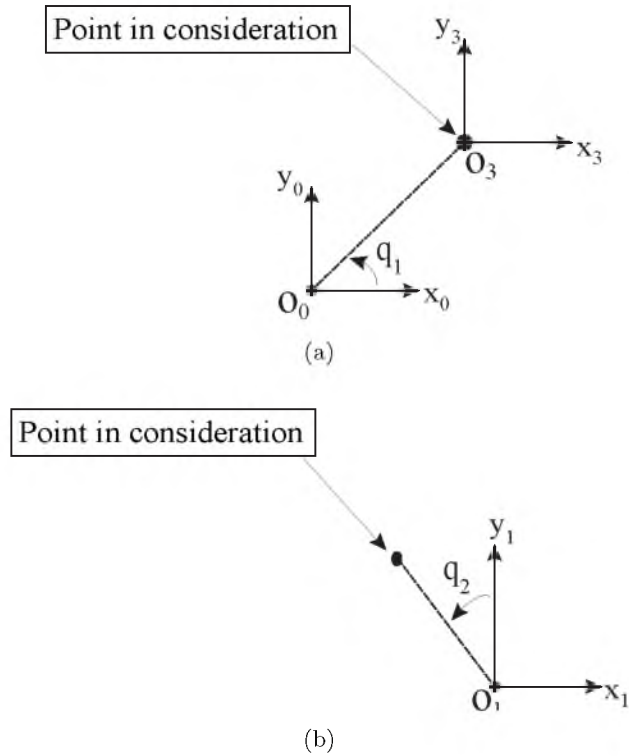
(A.10)

Figure A.1. Solving the inverse kinematics problem utilizing the (a) Top view, and (b) Front view.

where τ_i is the *generalized force* associated with the generalized coordinate q_i. Equation A.10 can be written in compact form as

$$\frac{d}{dt}\left(\frac{\partial L}{\partial \dot{\vec{q}}}\right)^T - \left(\frac{\partial L}{\partial \vec{q}}\right)^T = \vec{\tau} \tag{A.11}$$

where for a manipulator with an open kinematic chain, the generalized coordinates are gathered in the vector of variables $\vec{q}$. The kinetic energy T and potential energy U of link i are computed as:

$$T_i = \frac{1}{2}m_{l_i}\dot{\vec{q}}^T J_P^{(l_i)T} J_P^{l_i}\dot{\vec{q}} + \frac{1}{2}\dot{\vec{q}}^T J_O^{(l_i)T}(^0I_{l_i})J_O^{l_i}\dot{\vec{q}} \tag{A.12}$$

$$U_i = -m_{l_i}\,^0\vec{g}^T\vec{p}_i \tag{A.13}$$

where $\vec{p}_i$ is the position vector of the center of mass m_{l_i} of link i with respect to the base frame, $^0I_{l_i}$ represents the inertia tensor of link i relative to the center of mass of link i when expressed in the base frame, and $^iI_{l_i}$ is the inertia tensor when expressed in the link's frame ($^iI_{l_i}$ is a constant inertia tensor). $^0I_{l_i}$ can be expressed in terms of $^iI_{l_i}$ as:

$$^0I_{l_i} = R_i\,^iI_{l_i}R_i^T \tag{A.14}$$

where R_i is the rotation matrix from the link i frame to the base frame. J_P and J_O are the position and orientation Jacobians, written with respect to some link i, and are computed as:

$$J_P^{(l_i)} = [\mathrm{j}_{P1}^{(l_i)}\cdots\mathrm{j}_{Pi}^{(l_i)}\quad 0\cdots 0] \tag{A.15}$$

$$J_O^{(l_i)} = [\mathrm{j}_{O1}^{(l_i)}\cdots\mathrm{j}_{Oi}^{(l_i)}\quad 0\cdots 0] \tag{A.16}$$

with

$$\vec{\mathrm{j}}_{Pj}^{(l_i)} = \begin{cases} \vec{z}_{j-1} & \text{for a prismatic joint} \\ \vec{z}_{j-1}\times(\vec{p}_{l_i}-\vec{p}_{Oi}) & \text{for a rotary joint} \end{cases} \tag{A.17}$$

$$\vec{\mathrm{j}}_{Oj}^{(l_i)} = \begin{cases} \vec{0} & \text{for a prismatic joint} \\ \vec{z}_{j-1} & \text{for a rotary joint} \end{cases} \tag{A.18}$$

and $^0\vec{g} = [g_1\quad g_2\quad g_3]^T$ is the gravity acceleration vector with respect to O_0.

The Coriolis terms (according to Lagrange) can be found as follows. The generic element of C is

$$c_{ij} = \sum_{k=1}^{n} c_{ijk}\dot{q}_k \tag{A.19}$$

where the coefficients

$$c_{ijk} = \frac{1}{2}\left(\frac{\partial M_{ij}}{\partial q_k} + \frac{\partial M_{ik}}{\partial q_j} - \frac{\partial M_{jk}}{\partial q_i}\right) \tag{A.20}$$

where M is the $n \times n$ inertia matrix for an n-joint manipulator.

A.3.1 Inertia Tensor Equation

Before formulating the equations for dynamics, we must compute the inertia tensor $^0I_{l_i}$ for all the three links of the manipulator. Let the constant inertia tensor be defined as

$$^iI_{l_i} = \begin{bmatrix} ^iI_{i11} & ^iI_{i12} & ^iI_{i13} \\ ^iI_{i21} & ^iI_{i22} & ^iI_{i23} \\ ^iI_{i31} & ^iI_{i32} & ^iI_{i33} \end{bmatrix} \tag{A.21}$$

Links 1 and 2 of the Kleindiek MM3A manipulator are both symmetric with respect to two planes passing through their respective centers of mass, and link 3 is symmetric with respect to all three planes passing through its center of mass, thus the inertia tensor $^iI_{l_i}$ is diagonal (i.e., all off-diagonal terms are equal to zero). The inertia tensor of link i with respect to the base frame can be expressed as:

$$^0I_{l_i} = \begin{bmatrix} ^0I_{i11} & ^0I_{i12} & ^0I_{i13} \\ ^0I_{i21} & ^0I_{i22} & ^0I_{i23} \\ ^0I_{i31} & ^0I_{i32} & ^0I_{i33} \end{bmatrix} \tag{A.22}$$

Combined with Eq. A.14, we compute the inertia tensor $^0I_{l_i}$ as:

$$^0I_{l_1} \equiv \begin{bmatrix} ^0I_{111} & ^0I_{112} & ^0I_{113} \\ ^0I_{121} & ^0I_{122} & ^0I_{123} \\ ^0I_{131} & ^0I_{132} & ^0I_{133} \end{bmatrix} = {}^0R_1 {}^1I_{l_1} {}^0R_1^T \tag{A.23}$$

where

$$^0I_{111} = {}^1I_{111}c_1^2 + {}^1I_{133}s_1^2 \tag{A.24}$$

$$^0I_{112} = {}^1I_{111}s_1c_1 - {}^1I_{133}s_1c_1 \tag{A.25}$$

$$^0I_{113} = 0 \tag{A.26}$$

$$^0I_{121} = {}^1I_{111}s_1c_1 - {}^1I_{133}s_1c_1 \tag{A.27}$$

$$^0I_{122} = {}^1I_{111}s_1^2 + {}^1I_{133}c_1^2 \tag{A.28}$$

$$^0I_{123} = 0 \tag{A.29}$$

$$^0I_{131} = 0 \tag{A.30}$$

$$^0I_{132} = 0 \tag{A.31}$$

$$^0I_{133} = {}^1I_{122} \tag{A.32}$$

Similarly,

$$^0I_{l_2} = \begin{bmatrix} ^0I_{211} & ^0I_{212} & ^0I_{213} \\ ^0I_{221} & ^0I_{222} & ^0I_{223} \\ ^0I_{231} & ^0I_{232} & ^0I_{233} \end{bmatrix} \equiv {}^0R_2 {}^2I_{l_2} {}^0R_2^T \tag{A.33}$$

where

$$^0I_{211} = {}^2I_{211}c_1^2c_2^2 + {}^2I_{222}s_1^2 + {}^2I_{233}c_1^2s_2^2 \tag{A.34}$$

$$^0I_{212} = {}^2I_{211}s_1c_1c_2^2 - {}^2I_{222}s_1c_1 + {}^2I_{233}s_1c_1s_2^2 \tag{A.35}$$

$$^0I_{213} = {}^2I_{211}c_1s_2c_2 - {}^2I_{233}c_1c_2s_2 \tag{A.36}$$

$$^0I_{221} = {}^2I_{211}s_1c_1c_2^2 - {}^2I_{222}s_1c_1 + {}^2I_{233}s_1c_1s_2^2 \tag{A.37}$$

$$^0I_{222} = {}^2I_{211}s_1^2c_2^2 + {}^2I_{222}c_1^2 + {}^2I_{233}s_1^2s_2^2 \tag{A.38}$$

$$^0I_{223} = {}^2I_{211}s_1s_2c_2 - {}^2I_{233}s_1s_2c_2 \tag{A.39}$$

$$^0I_{231} = {}^2I_{211}s_2c_1c_2 - {}^2I_{233}c_1s_2c_2 \tag{A.40}$$

$$^0I_{232} = {}^2I_{211}s_1s_2c_2 - {}^2I_{233}s_1s_2c_2 \tag{A.41}$$

$$^0I_{233} = {}^2I_{211}s_2^2 + {}^2I_{233}c_2^2 \tag{A.42}$$

and

$$^0I_{l_3} = \begin{bmatrix} {}^0I_{311} & {}^0I_{312} & {}^0I_{313} \\ {}^0I_{321} & {}^0I_{322} & {}^0I_{323} \\ {}^0I_{331} & {}^0I_{332} & {}^0I_{333} \end{bmatrix} \equiv {}^0R_3 {}^3I_3 {}^0R_3^T \tag{A.43}$$

where all the elements of $^0I_{l_3}$ are analogous to those of $^0I_{l_2}$ (since $^0R_3 = {}^0R_2$), except that the elements of $^2I_{l_2}$ are replaced by $^3I_{l_3}$.

A.3.2 Derivation of Dynamic Equation

The mass of link i is expressed as m_i. We formulate the position and orientation Jacobians as follows. For link 1, we assume that m_1 is located at a distance r_1 from O_0 along $\vec{x}_1$, and calculate:

$$J_P^{(l_1)} = \begin{bmatrix} -r_1s_1 & 0 & 0 \\ r_1c_1 & 0 & 0 \\ 0 & 0 & 0 \end{bmatrix} \tag{A.44}$$

$$J_O^{(l_1)} = \begin{bmatrix} 0 & 0 & 0 \\ 0 & 0 & 0 \\ 1 & 0 & 0 \end{bmatrix} \tag{A.45}$$

For link 2, we assume that m_2 is located at a distance r_2 from O_1 along $\vec{z}_2$, and calculate:

$$J_P^{(l_2)} = \begin{bmatrix} -a_1s_1 + r_2s_1s_2 & -r_2c_1c_2 & 0 \\ a_1c_1 - r_2c_1s_2 & -r_2s_1c_2 & 0 \\ 0 & -r_2s_2 & 0 \end{bmatrix} \tag{A.46}$$

$$J_O^{(l_2)} = \begin{bmatrix} 0 & s_1 & 0 \\ 0 & -c_1 & 0 \\ 1 & 0 & 0 \end{bmatrix} \tag{A.47}$$

For link 3, we use a different convention, and assume that m_3 is located at a distance r_3 from O_3 along $-\vec{z}_3$, and calculate:

$$J_P^{(l_3)} = \begin{bmatrix} (l_2 + q_3 - r_3)s_1s_2 - a_1s_1 & -(l_2 + q_3 - r_3)c_1c_2 & -c_1s_2 \\ -(l_2 + q_3 - r_3)c_1s_2 + a_1c_1 & -(l_2 + q_3 - r_3)s_1c_2 & -s_1s_2 \\ 0 & -(l_2 + q_3 - r_3)s_2 & c_2 \end{bmatrix} \tag{A.48}$$

$$J_O^{(l_3)} = \begin{bmatrix} 0 & s_1 & 0 \\ 0 & -c_1 & 0 \\ 1 & 0 & 0 \end{bmatrix} \tag{A.49}$$

Next, we compute the kinetic and potential energy. In the case of link 1,

$$T_1 = \frac{1}{2}m_1 r_1^2 \dot{q}_1^2 + \frac{1}{2}{}^0I_{133}\dot{q}_1^2 \tag{A.50}$$

$$U_1 = -m_1 r_1 g_1 c_1 - m_1 r_1 g_2 s_1 \tag{A.51}$$

and for link 2,

$$\begin{aligned} T_2 &= \frac{1}{2}m_2(a_1 - r_2s_2)^2\dot{q}_1^2 + \frac{1}{2}m_2 r_2^2 \dot{q}_2^2 + \frac{1}{2}[{}^0I_{233}\dot{q}_1^2 + \dot{q}_2^2({}^0I_{211}s_1^2 \\ &\quad + {}^0I_{222}c_1^2 - ({}^0I_{221} + {}^0I_{212})s_1c_1) + \dot{q}_1\dot{q}_2({}^0I_{213}s_1 - {}^0I_{223}c_1 \\ &\quad + {}^0I_{231}s_1 - {}^0I_{232}c_1)] \end{aligned} \tag{A.52}$$

$$U_2 = -m_2 g_1(a_1c_1 - r_2c_1s_2) - m_2 g_2(a_1s_1 - r_2s_1s_2) - m_2 g_3 r_2 c_2 \tag{A.53}$$

and for link 3,

$$\begin{aligned} T_3 &= \frac{1}{2}m_3[(a_1 - (l_2 + q_3 - r_3)s_2)^2\dot{q}_1^2 + (l_2 + q_3 - R)^2\dot{q}_2^2 + \dot{q}_3^2] + \\ &\quad \frac{1}{2}[{}^0I_{333}\dot{q}_1^2 + \dot{q}_2^2({}^0I_{311}s_1^2 + {}^0I_{322}c_1^2 - ({}^0I_{321} + {}^0I_{312})s_1c_1) \\ &\quad + \dot{q}_1\dot{q}_2({}^0I_{313}s_1 - {}^0I_{323}c_1 + {}^0I_{331}s_1 - {}^0I_{332}c_1)] \end{aligned} \tag{A.54}$$

$$\begin{aligned} U_3 &= -m_3 g_1(a_1c_1 - (l_2 + q_3 - r_3)c_1s_2) \\ &\quad -m_3 g_2(a_1s_1 - (l_2 + q_3 - r_3)s_1s_2) - m_3 g_3(l_2 + q_3 - r_3)c_2 \end{aligned} \tag{A.55}$$

The Lagrangian becomes:

$$L = \sum_{i=1}^{3} T_i - \sum_{i=1}^{3} U_i \tag{A.56}$$

Proceeding with equation A.10, we first formulate the inertial terms. For link 1:

$$\frac{\partial L}{\partial \dot{q}_1} = \dot{q}_1[m_1 r_1^2 + {}^0I_{133} + {}^0I_{233} + {}^0I_{333} + m_2(a_1 - r_2 s_2)^2 + m_3(a_1$$
$$- (l_2 + q_3 - r_3)s_2)^2] + 0.5\ddot{q}_2[s1({}^0I_{213} + {}^0I_{231} + {}^0I_{313} + {}^0I_{331})$$
$$- c_1({}^0I_{223} + {}^0I_{232} + {}^0I_{323} + {}^0I_{332})] \tag{A.57}$$

$$\frac{d}{dt}\frac{\partial L}{\partial \dot{q}_1} = \ddot{q}_1[m_1 r_1^2 + {}^0I_{133} + {}^0I_{233} + {}^0I_{333} + m_2(a_1 - r_2 s_2)^2 + m_3(a_1$$
$$- (l_2 + q_3 - r_3)s_2)^2] + 0.5\ddot{q}_2[s1({}^0I_{213} + {}^0I_{231} + {}^0I_{313}$$
$$+ {}^0I_{331}) - c_1({}^0I_{223} + {}^0I_{232} + {}^0I_{323} + {}^0I_{332})] \tag{A.58}$$

For link 2:

$$\frac{\partial L}{\partial \dot{q}_2} = 0.5\dot{q}_1[s_1({}^0I_{213} + {}^0I_{231} + {}^0I_{313} + {}^0I_{331}) - c_1({}^0I_{223} + {}^0I_{232}$$
$$+ {}^0I_{323} + {}^0I_{332})] + \dot{q}_2[m_2 r_2^2 + s_1^2({}^0I_{311} + {}^0I_{211}) + c_1^2({}^0I_{322}$$
$$+ {}^0I_{222}) - s_1 c_1({}^0I_{321} + {}^0I_{312} + {}^0I_{221} + {}^0I_{212})] + m_3\dot{q}_2(l_2 + q_3$$
$$- r_3)^2 \tag{A.59}$$

$$\frac{d}{dt}\frac{\partial L}{\partial \dot{q}_2} = 0.5\ddot{q}_1[s_1({}^0I_{213} + {}^0I_{231} + {}^0I_{313} + {}^0I_{331}) - c_1({}^0I_{223} + {}^0I_{232} + {}^0I_{323}$$
$$+ {}^0I_{332})] + \ddot{q}_2[m_2 r_2^2 + s_1^2({}^0I_{311} + {}^0I_{211}) + c_1^2({}^0I_{322} + {}^0I_{222})$$
$$- s_1 c_1({}^0I_{321} + {}^0I_{312} + {}^0I_{221} + {}^0I_{212})] + m_3\ddot{q}_2(l_2 + q_3 - r_3)^2 \tag{A.60}$$

and for link 3:

$$\frac{\partial L}{\partial \dot{q}_3} = m_3\dot{q}_3 \tag{A.61}$$

$$\frac{d}{dt}\frac{\partial L}{\partial \dot{q}_3} = m_3\ddot{q}_3 \tag{A.62}$$

From equation A.61,A.59, and A.57, we can formulate the inertia matrix

$$M = \begin{bmatrix} M_{11} & M_{12} & M_{13} \\ M_{21} & M_{22} & M_{23} \\ M_{31} & M_{32} & M_{33} \end{bmatrix} \tag{A.63}$$

where

$$M_{11} = m_1 r_1^2 + {}^0I_{133} + {}^0I_{233} + {}^0I_{333} + m_2(a_1 - r_2 s_2)^2$$
$$+ m_3(a_1 - (l_2 + q_3 - r_3)s_2)^2 \tag{A.64}$$

$$M_{12} = 0.5[s_1({}^0I_{213} + {}^0I_{231} + {}^0I_{313} + {}^0I_{331})$$
$$- c_1({}^0I_{223} + {}^0I_{232} + {}^0I_{323} + {}^0I_{332})] \tag{A.65}$$

$$M_{13} = 0 \tag{A.66}$$

$$M_{21} = 0.5[s_1({}^0I_{213} + {}^0I_{231} + {}^0I_{313} + {}^0I_{331})$$
$$- c_1({}^0I_{223} + {}^0I_{232} + {}^0I_{323} + {}^0I_{332})] \tag{A.67}$$

$$M_{22} = m_2 r_2^2 + s_1^2({}^0I_{311} + {}^0I_{211}) + c_1^2({}^0I_{322} + {}^0I_{222})$$
$$- s_1 c_1({}^0I_{321} + {}^0I_{312} + {}^0I_{221} + {}^0I_{212}) + m_3(l_2 + q_3 - r_3)^2 \tag{A.68}$$

$$M_{23} = 0 \tag{A.69}$$

$$M_{31} = 0 \tag{A.70}$$

$$M_{32} = 0 \tag{A.71}$$

$$M_{33} = m_3 \tag{A.72}$$

Next, we formulate the centrifugal and coriolis terms. We first calculate the *Christoffel symbols of the first kind, c_{ijk}*, as defined in equation A.20.

For link 1:

$$c_{111} = \frac{1}{2}\left(\frac{\partial \mathbf{M}_{11}}{\partial q_1} + \frac{\partial \mathbf{M}_{11}}{\partial q_1} - \frac{\partial \mathbf{M}_{11}}{\partial q_1}\right) = 0 \tag{A.73}$$

$$c_{112} = \frac{1}{2}\left(\frac{\partial \mathbf{M}_{11}}{\partial q_2} + \frac{\partial \mathbf{M}_{12}}{\partial q_1} - \frac{\partial \mathbf{M}_{12}}{\partial q_1}\right)$$
$$= s_2 c_2({}^2I_{211} + {}^3I_{311} - {}^2I_{233} - {}^3I_{333}) - m_2 r_2 c_2(a_1 - r_2 s_2)$$
$$+ m_3(s_2 c_2(l_2 + q_3 - r_3)^2 - a_1 c_2(l_2 + q_3 - r_3)) \tag{A.74}$$

$$c_{113} = \frac{1}{2}\left(\frac{\partial \mathbf{M}_{11}}{\partial q_3} + \frac{\partial \mathbf{M}_{13}}{\partial q_1} - \frac{\partial \mathbf{M}_{13}}{\partial q_1}\right)$$
$$= m_3(l_2 + q_3 - r_3)s_2^2 - m_3 a_1 s_2 \tag{A.75}$$

$$+ m_2 r_2 c_2 (a_1 - r_2 s_2) - m_3 (s_2 c_2 (l_2 + q_3 - r_3)^2$$

$$- a_1 c_2 (l_2 + q_3 - r_3))$$

$$c_{212} = \frac{1}{2} \left(\frac{\partial M_{21}}{\partial q_2} + \frac{\partial M_{22}}{\partial q_1} - \frac{\partial M_{12}}{\partial q_1} \right) = 0 \tag{A.82}$$

$$c_{213} = \frac{1}{2} \left(\frac{\partial M_{21}}{\partial q_3} + \frac{\partial M_{23}}{\partial q_1} - \frac{\partial M_{13}}{\partial q_1} \right) = 0 \tag{A.83}$$

$$c_{221} = \frac{1}{2} \left(\frac{\partial M_{22}}{\partial q_1} + \frac{\partial M_{21}}{\partial q_1} - \frac{\partial M_{21}}{\partial q_2} \right) = 0 \tag{A.84}$$

$$c_{222} = \frac{1}{2} \left(\frac{\partial M_{22}}{\partial q_2} + \frac{\partial M_{22}}{\partial q_2} - \frac{\partial M_{22}}{\partial q_2} \right) = 0 \tag{A.85}$$

$$c_{223} = \frac{1}{2} \left(\frac{\partial M_{22}}{\partial q_3} + \frac{\partial M_{23}}{\partial q_2} - \frac{\partial M_{23}}{\partial q_2} \right) = m_3 (l_2 + q_3 - r_3) \tag{A.86}$$

$$c_{231} = 0 \tag{A.87}$$

$$c_{232} = \frac{1}{2} \left(\frac{\partial M_{23}}{\partial q_2} + \frac{\partial M_{22}}{\partial q_3} - \frac{\partial M_{32}}{\partial q_2} \right) = m_3 (l_2 + q_3 - r_3) \tag{A.88}$$

$$c_{233} = 0 \tag{A.89}$$

$$\tag{A.90}$$

$$c_{121} = \frac{1}{2}\left(\frac{\partial \mathbf{M}_{12}}{\partial q_1} + \frac{\partial \mathbf{M}_{11}}{\partial q_2} - \frac{\partial \mathbf{M}_{21}}{\partial q_2}\right)$$

$$= s_2 c_2({}^2I_{211} + {}^3I_{311} - {}^2I_{233} - {}^3I_{333}) - m_2 r_2 c_2(a_1 - r_2 s_2)$$

$$+ m_3(s_2 c_2(l_2 + q_3 - r_3)^2 - a_1 c_2(l_2 + q_3 - r_3)) \tag{A.76}$$

$$c_{122} = \frac{1}{2}\left(\frac{\partial \mathbf{M}_{12}}{\partial q_2} + \frac{\partial \mathbf{M}_{12}}{\partial q_2} - \frac{\partial \mathbf{M}_{22}}{\partial q_1}\right) = 0 \tag{A.77}$$

$$c_{123} = \frac{1}{2}\left(\frac{\partial \mathbf{M}_{12}}{\partial q_3} + \frac{\partial \mathbf{M}_{13}}{\partial q_2} - \frac{\partial \mathbf{M}_{23}}{\partial q_1}\right) = 0 \tag{A.78}$$

$$c_{131} = \frac{1}{2}\left(\frac{\partial \mathbf{M}_{13}}{\partial q_1} + \frac{\partial \mathbf{M}_{11}}{\partial q_3} - \frac{\partial \mathbf{M}_{31}}{\partial q_1}\right)$$

$$= m_3(l_2 + q_3 - r_3)s_2^2 - m_3 a_1 s_2 \tag{A.79}$$

$$c_{132} = \frac{1}{2}\left(\frac{\partial \mathbf{M}_{13}}{\partial q_2} + \frac{\partial \mathbf{M}_{12}}{\partial q_3} - \frac{\partial \mathbf{M}_{32}}{\partial q_1}\right) = 0 \tag{A.80}$$

$$c_{133} = \frac{1}{2}\left(\frac{\partial \mathbf{M}_{13}}{\partial q_3} + \frac{\partial \mathbf{M}_{13}}{\partial q_3} - \frac{\partial \mathbf{M}_{33}}{\partial q_1}\right) = 0 \tag{A.81}$$

For link 2:

$$c_{211} = \frac{1}{2}\left(\frac{\partial \mathbf{M}_{21}}{\partial q_1} + \frac{\partial \mathbf{M}_{21}}{\partial q_1} - \frac{\partial \mathbf{M}_{11}}{\partial q_2}\right)$$

$$= -0.5[2s_2 c_2({}^2I_{211} + {}^3I_{311} - {}^2I_{233} - {}^3I_{333})]$$

For link 3:

$$c_{311} = \frac{1}{2}\left(\frac{\partial M_{31}}{\partial q_1} + \frac{\partial M_{31}}{\partial q_1} - \frac{\partial M_{11}}{\partial q_3}\right)$$

$$= -m_3(l_2 + q_3 - r_3)s_2^2 + m_3a_1s_2 \tag{A.91}$$

$$c_{312} = 0 \tag{A.92}$$

$$c_{313} = 0 \tag{A.93}$$

$$c_{321} = 0 \tag{A.94}$$

$$c_{322} = \frac{1}{2}\left(\frac{\partial M_{32}}{\partial q_2} + \frac{\partial M_{32}}{\partial q_2} - \frac{\partial M_{22}}{\partial q_3}\right) = m_3(l_2 + q_3 - r_3) \tag{A.95}$$

$$c_{323} = 0 \tag{A.96}$$

$$c_{331} = 0 \tag{A.97}$$

$$c_{332} = 0 \tag{A.98}$$

$$c_{333} = 0 \tag{A.99}$$

Thus, the coriolis and centrifugal terms can be computed as:

$$C = \begin{bmatrix} C_{11} & C_{12} & C_{13} \\ C_{21} & C_{22} & C_{23} \\ C_{31} & C_{32} & C_{33} \end{bmatrix} \tag{A.100}$$

with

$$C_{11} = \dot{q}_1c_{111} + \dot{q}_2c_{112} + \dot{q}_3c_{113}$$

$$= \dot{q}_2[s_2c_2(^2I_{211} + {}^3I_{311} - {}^2I_{233} - {}^3I_{333}) - m_2r_2c_2(a_1 - r_2s_2)$$

$$+m_3(s_2c_2(l_2 + q_3 - r_3)^2 - a_1c_2(l_2 + q_3 - r_3))]$$

$$+\dot{q}_3[m_3(l_2 + q_3 - r_3)s_2^2 - m_3a_1s_2] \tag{A.101}$$

$$C_{12} = \dot{q}_1c_{121} + \dot{q}_2c_{122} + \dot{q}_3c_{123}$$

$$= \dot{q}_1[s_2c_2(^2I_{211} + {}^3I_{311} - {}^2I_{233} - {}^3I_{333}) - m_2r_2c_2(a_1 - r_2s_2)$$

$$+m_3(s_2c_2(l_2 + q_3 - r_3)^2 - a_1c_2(l_2 + q_3 - r_3))] \tag{A.102}$$

$$C_{13} = \dot{q}_1c_{131} + \dot{q}_2c_{132} + \dot{q}_3c_{133}$$

$$= \dot{q}_1[m_3(l_2 + q_3 - r_3)s_2^2 - m_3a_1s_2] \tag{A.103}$$

$$C_{21} = \dot{q}_1c_{211} + \dot{q}_2c_{212} + \dot{q}_3c_{213}$$

$$= \dot{q}_1[-0.5[2s_2c_2(^2I_{211} + {}^3I_{311} - {}^2I_{233} - {}^3I_{333})] + m_2r_2c_2(a_1$$

$$-r_2s_2) - m_3(s_2c_2(l_2 + q_3 - r_3)^2 - a_1c_2(l_2 + q_3 - r_3))] \tag{A.104}$$

$$
\begin{aligned}
C_{22} &= \dot{q}_1 c_{221} + \dot{q}_2 c_{222} + \dot{q}_3 c_{223} \\
&= \dot{q}_3 [m_3(l_2 + q_3 - r_3)]
\end{aligned}
\tag{A.105}
$$

$$
\begin{aligned}
C_{23} &= \dot{q}_1 c_{231} + \dot{q}_2 c_{232} + \dot{q}_3 c_{233} \\
&= \dot{q}_2 [m_3(l_2 + q_3 - r_3)]
\end{aligned}
\tag{A.106}
$$

$$
\begin{aligned}
C_{31} &= \dot{q}_1 c_{311} + \dot{q}_2 c_{312} + \dot{q}_3 c_{313} \\
&= \dot{q}_1 [-m_3(l_2 + q_3 - r_3)s_2^2 + m_3 a_1 s_2]
\end{aligned}
\tag{A.107}
$$

$$
\begin{aligned}
C_{32} &= \dot{q}_1 c_{321} + \dot{q}_2 c_{322} + \dot{q}_3 c_{323} \\
&= \dot{q}_2 [m_3(l_2 + q_3 - r_3)]
\end{aligned}
\tag{A.108}
$$

$$
\begin{aligned}
C_{33} &= \dot{q}_1 c_{331} + \dot{q}_2 c_{332} + \dot{q}_3 c_{333} \\
&= 0
\end{aligned}
\tag{A.109}
$$

Next, we formulate the gravity terms:

$$
G(\vec{q}) = \begin{bmatrix} G_1 \\ G_2 \\ G_3 \end{bmatrix}
\tag{A.110}
$$

with

$$
\begin{aligned}
G_1 &= \frac{\partial U}{\partial q_1} \\
&= m_1 r_1 g_1 s_1 - m_1 r_1 g_2 c_1 + m_2 g_1 (a_1 s_1 - r_2 s_1 s_2) - m_2 g_2 (a_1 c_1 \\
&\quad - r_2 c_1 s_2) + m_3 g_1 (a_1 s_1 - (l_2 + q_3 - r_3)s_1 s_2) - m_3 g_2 (a_1 c_1 \\
&\quad - (l_2 + q_3 - r_3)c_1 s_2)
\end{aligned}
\tag{A.111}
$$

$$
\begin{aligned}
G_2 &= \frac{\partial U}{\partial q_2} \\
&= m_2 r_2 g_1 c_1 c_2 + m_2 r_2 g_2 s_1 c_2 + m_2 g_3 r_2 s_2 + m_3(l_2 + q_3 - r_3)g_1 c_1 c_2 \\
&\quad + m_3(l_2 + q_3 - r_3)g_2 s_1 c_2 + m_3 g_3 (l_2 + q_3 - r_3)s_2
\end{aligned}
\tag{A.112}
$$

$$
\begin{aligned}
G_3 &= \frac{\partial U}{\partial q_3} \\
&= m_3 g_1 c_1 s_2 + m_3 g_2 s_1 s_2 - m_3 g_3 c_2
\end{aligned}
\tag{A.113}
$$

Using the inertial, coriolis, and gravitational terms formulated above, as well as the Jacobian, we compute the equation for the dynamics of the MM3A as:

$$
M(\vec{q})\ddot{\vec{q}} + C(\vec{q}, \dot{\vec{q}})\dot{\vec{q}} + G(\vec{q}) - J^T(\vec{q})\vec{f} = \vec{\tau}
\tag{A.114}
$$

REFERENCES

[1] J. M. Breguet, R. Perez, A. Bergander, C. Schmitt, R. Clavel, and H. Bleuler. Piezoactuators for motion control from centimeter to nanometer. In *Proc. IEEE/RSJ Int. Conf. Intelligent Robots and Systems*, pages 492–497, 2000.

[2] J. M. Breguet, W. Driesen, F. Kaegi, and T. Cimprich. Applications of piezo-actuated micro-robots in micro-biology and material science. In *Int. Conf. Mechatronics and Automation*, pages 57–62, 2007.

[3] P. Dario, R. Valleggi, M. C. Carrozza, M. C. Montesi, and M. Cocco. Microactuators for microrobots: a critical curvey. *Review Literature and Arts of the Americas*, 2(3):141–157, 1992.

[4] C. Edeler and S. Fatikow. Open loop force control of piezo-actuated stick-slip drives. *Int. J. Intelligent Mechatronics and Robotics*, 1(1):1–19, 2011.

[5] M. Rakotondrabe, Y. Haddab, and P. Lutz. Development, modeling and control of a micro-/nanopositioning 2-dof stick-slip device. *IEEE/ASME Trans. Mechatronics*, 14(6):733–745, 2009.

[6] Kleindiek Nanotechnik GmbH. *System manual, MM3A micromanipulator system*, 2006.

[7] T. Higuchi and Y. Yamagata. Micro robot arm utilizing rapid deformation of piezo-electric elements. *Advanced Robotics*, 6(3):353–360, 1992.

[8] S. Kleindiek. Electromechanical positioning unit. "United States Patent", 1999.

[9] Physik Instrumente. "http://www.physikinstrumente.com".

[10] Nanocontrol. "http://www.nanocontrol.co.jp".

[11] Nanomotion. "http://www.nanomotion.com".

[12] Smaract GmbH. "http://www.smaract.de".

[13] PiezoMotor. "http://www.piezomotor.com".

[14] Kleindiek Nanotechnik MM3A. "http://www.nanotechnik.com/".

[15] Zyvex Nanomanipulator. "http://www.zyvex.com/".

[16] Imina Techonologies miBot. "http://www.imina.ch/".

[17] Attocube Nanopositioners. "http://www.attocube.com/".

[18] J. Y. Peng and X. B. Chen. Modeling of piezoelectric-driven stick-slip actuators. *IEEE/ASME Trans. Mechatronics*, 16(2):394–399, 2011.

[19] J. W. Li, G. S. Yang, W. J. Zhang, S. D. Tu, and X. B. Chen. Thermal effect on piezo-electric stick-slip actuator systems. *Review of Scientific Instruments*, 79(4):046108, 2008.

[20] Q. Zhou, C. Corral, P. J. Esteban, A. Aurelian, and H. N. Koivo. Environmental influences on microassembly. In *Proc. IEEE/RSJ Int. Conf. Intelligent Robots and Systems*, pages 1760–1765, 2002.

[21] E. Rabinowicz. The intrinsic variables affecting the stick-slip process. *Proc. Phyical Society*, 71(4):668–675, 1958.

[22] R. Saeidpourazar and N. Jalili. Nano-robotic manipulation using a RRP nanomanip-ulator: Part A- mathematical modeling and development of a robust adaptive driving mechanism. *Applied Mathematics and Computation*, 206(2):618–627, 2008.

[23] R. Saeidpourazar and N. Jalili. Nano-robotic manipulation using a RRP nanomanip-ulator: Part B- Robust control of manipulator's tip using fused visual servoing and force sensor feedbacks. *Applied Mathematics and Computation*, 206(2):628–642, 2008.

[24] R. Yang, N. Xi, K. Lai, B. Gao, H. Chen, C. Su, and J. Shi. Motion controller for the atomic force microscopy based nanomanipulation system. In *Proc. IEEE/RSJ Int. Conf. Intelligent Robots and Systems*, pages 1339–1344, 2009.

[25] M. Rakotondrabe, Y. Haddab, and P. Lutz. Voltage/frequency proportional control of stick-slip micropositioning systems. *IEEE Trans. Control Systems Technology*, 16(6):1316–1322, 2008.

[26] B. Sedghi. Control design of hybrid systems via dehybridization. *PhD thesis No. 2859, EPFL*, 2003.

[27] H. Liaw, B. Shirinzadeh, and J. Smith. Enhanced sliding mode motion tracking control of piezoelectric actuators. *Sensors and Actuators: Physical*, 138(1):194–202, 2007.

[28] B. E. Kratochvil, L. Dong, and B. J. Nelson. Real time rigid-body visual tracking in a scanning electron microscope. *Int. J. Robotics Research*, 28(4):488–511, 2009.

[29] H. Hötzendorfer, I. Giouroudi, S. Bou, and M. Ferros. Evaluation of different control algorithms for a micromanipulation system. In *Int. Conf. Engineering and Mathematics*, 2006.

[30] S. Fatikow and V. Eichhorn. Nanohandling automation: trends and current develop-ments. *J. Mechanical Engineering Science*, 222(7):1353–1369, 2008.

[31] Victor Birman. Physically nonlinear behavior of piezoelectric actuators subject to high electric fields. Technical report, University of Missouri-Rolla, St. Louis, Missouri, 2005.

[32] C. Edeler, I. Meyer, and S. Fatikow. Modeling of stick-slip micro-drives. *J. Micro-Nano Mechatronics*, pages 1–23, 2011.

[33] A. J. Lockwood, J. J. Wang, R. Gay, and B. J. Inkson. Characterising performance of tem compatible nanomanipulation slip-stick inertial sliders against gravity. *J. Physics: Conference Series*, 126:012096, 2008.

[34] M. Nambi, A. Damani, and J. J. Abbott. Toward intuitive teleoperation of micro/nano-manipulators with piezoelectric stick-slip actuators. In *Proc. IEEE/RSJ Int. Conf. Intelligent Robots and Systems*, pages 445–450, 2011.

[35] F. Al-Bender and K. De Moerlooze. On the relationship between normal load and friction force in pre-sliding frictional contacts. part 1: Theoretical analysis. *Wear*, 269(3-4):174–182, 2010.

[36] K. De Moerlooze and F. Al-Bender. On the relationship between normal load and friction force in pre-sliding frictional contacts. part 2: Experimental investigation. *Wear*, 269(3-4):183–189, 2010.

[37] D. W. Pohl. Dynamic piezoelectric translation devices. *Review of Scientific Instruments*, 58(1):54–57, 1987.

[38] S. H. Chang and S. S. Li. A high resolution long travel friction-drive micropositioner with programmable step size. *Review of Scientific Instruments*, 70(6):2776–2782, 1999.

[39] J. Swevers, F. Al-Bender, C. G. Ganseman, and T. Prajogo. An integrated friction model structure with improved presliding behavior for accurate friction compensation. *IEEE Trans. Automatic Control*, 45(4):675–686, 2000.

[40] P. R. Dahl. Single state elasto-plastic friction models. Technical report, The Aerospace Corporation, El Segunda, California, 1968.

[41] P. Dupont, V. Hayward, and B. Armstrong. Single state elasto-plastic friction models. *IEEE Trans. Automatic Control*, 47(5):787–792, 2002.

[42] C. Canudas de Wit, H. Olsson, K. J. Astrom, and P. Lischinsky. A new model for control of systems with friction. *IEEE Trans. Automatic Control*, 40(3):419–425, 1995.

[43] M. Goldfarb and N. Celanovic. Modeling piezoelectric stack actuators for control of micromanipulation. *IEEE Control Systems*, 17(3):69–79, 1997.

[44] B. J. Lazan. *Damping of materials and members in structural mechanics*. Pergamon Press, London, 1968.

[45] H. J. M. T. S. Adriaens, W. L. De Koning, and R. Banning. Modeling piezoelectric actuators. *IEEE/ASME Trans. Mechatronics*, 5(4):331–341, 2000.

[46] X. B. Chen, Q. S. Zhang, D. Kang, and W. J. Zhang. On the dynamics of piezoactuated positioning systems. *Review of Scientific Instruments*, 79(11):116101, 2008.

[47] J. M. Breguet and R. Clavel. Stick and slip actuators: design, control, performances and applications. *Int. Symp. on Micromechatronics and Human Science. - Creation of New Industry*, pages 89–95, 1998.

[48] A. Bergander and J. M. Breguet. Performance improvements for stick-slip positioners. *Int. Symp. on Micromechatronics and Human Science*, pages 59–66, 2003.

[49] W. Zesch, R. Bÿchi, A. Codourey, and R. Siegwart. Inertial drives for micro- and nanorobots : Two novel mechanisms. *Proc. SPIE*, 2593:80–88, 1995.

[50] A. K. Eigoli and G. Vossoughi. Dynamic modeling of stick-slip motion in a legged, piezoelectric driven microrobot. *Advanced Robotic*, 7(3):201–208, 2010.

[51] J. W. Li, G. S. Yang, W. J. Zhang, S. D. Tu, and X. B. Chen. Thermal effect on piezoelectric stick-slip actuator systems. *Review of Scientific Instruments*, 79(4):046108, 2008.

[52] J. W. Li, X. B. Chen, Q. An, S. D. Tu, and W. J. Zhang. Friction models incorporating thermal effects in highly precision actuators. *Review of Scientific Instruments*, 80(4):045104, 2009.

[53] R. Cain, N. Page, and S. Biggs. Microscopic and macroscopic aspects of stick-slip motion in granular shear. *Physical Review E*, 64(1):1–8, 2001.

[54] B. Siciliano, L. Sciavicco, L. Villani, and G. Oriolo. *Robotics modelling, planning and control.* Springer, UK, 2008.